

**Variations in Subsidence along the Gulf of Mexico passive margin from
Airborne-LiDAR data and Time Series InSAR.**

PhD Prospectus.

Student: Diana Carolina Hurtado-Pulido

Department: Earth and Environmental Science Department. Tulane University

Dissertation Director: Dr. Cynthia Ebinger

Dissertation Committee: Dr. Nicole Gasparini, Dr. Kathryn Materna, Dr. Jennifer Whitten.

November/2023

Variations in Subsidence along the Gulf of Mexico passive margin from Airborne-LiDAR data and Time Series InSAR

D. Carolina Hurtado-Pulido

INTRODUCTION

Quantification of vertical land displacement is an important issue in coastal areas due to ongoing sea level rise and its consequences on the community and ecosystems. Global Mean Sea Level (GMSL) rise has been mainly attributed to thermal and mass changes in the ocean during the last century and had an average rate of 1.56 ± 0.33 mm/y (Frederikse et al., 2020), it has been estimated to reach a rate of ~ 3 mm/y by 2100 (Nerem et al., 2018). However, satellite altimetry already shows rates of 3-3.2 mm/y between 1993-2021 (Church and White, 2011; Blunden et al., 2022). Temporally, GMSL rates have increased over time, tide gauge records show that the GMSL rate has accelerated from 1.1 ± 0.7 mm/y between 1880-1935 to 1.8 ± 0.3 mm/y between 1936-2009 with peaks in the 1940s, 1970s, and 1990s related to melting of ice caps, glacier, and Greenland, and thermal expansion (Church and White, 2011). Nevertheless, Relative Sea Level (RSL), which includes the sea-level rise and vertical land displacement, is often not considered in most of these global projections due to the complexity of each region but is highly important at local and regional length scales to fully estimate the effects of sea-level rise at each location (e.g., Shirzaei, et al., 2021). RSL across the Gulf of Mexico (GOM) has large variations because there are different contributors to vertical elevation changes (subsidence and uplifting) that vary spatially and temporally across the area (e.g., NASEM 2018). These processes can be separated into natural processes such as compaction of recent sediments (6.4- 9 mm/y - e.g., Keogh and Törnqvist, 2019; Nienhuis et al., 2017), isostatic adjustments (glacial – 0.32 mm/y e.g., Love et al., 2016, sediment – <0.5 mm/y e.g., Wolstencroft et al., 2014), faulting (3 mm/y e.g., Hopkins et al., 2021), and anthropogenic processes such as extraction and injection of fluids (25-50 mm/y e.g., Jones et al., 2016) (e.g., NASEM 2018; Shirzaei, et al., 2021).

Vertical displacement has been studied previously using diverse methods to quantify the rates of these drivers (Shirzaei, et al., 2021). Isostatic adjustments may lead to long-term subsidence along the east coast of North America (Karegar et al., 2017) and are mainly studied using numerical models (e.g., Love et al., 2016; Wolstencroft et al., 2014). Shallow processes like compaction and compression of Holocene sediments are the primary factors causing subsidence on the Mississippi delta, and in areas close to the shoreline, these have been analyzed with different methods such as rod surface-elevation table and GNSS interferometric reflectometry (e.g., Keogh and Törnqvist, 2019; Karegar et al., 2020). Fault slip and creep are difficult to quantify in the GOM because they can be episodic and slow, and the signal can be masked by faster processes (Gagliano et al., 2003), some of the methods used are optically stimulated luminescence dating and GNSS real-time kinematic positioning (Shen et al., 2017; Hopkins et al., 2021). Extraction and injection of fluids can change pore pressure at depth and result in irreversible sediment compaction or uplift respectively (Jones et al., 2016; Shirzaei et al., 2016), and subsequently, faults may move, and, in some cases, this could trigger seismic activity (Shirzaei et al., 2016; Shirzaei et al., 2021).

For this research, I tested geodetic methods (Light Detection And Ranging – LiDAR, Interferometric Synthetic Aperture Radar – InSAR and InSAR time series) to measure displacement due to different mechanisms in different areas across the GOM for the last decades. The study areas for this investigation are in the GOM, then they have similar tectonic setting and have fluid extraction and injection activities, but they differ in distance to the shoreline and therefore the processes causing displacement may be different. LiDAR data has been used before to quantify displacement caused by earthquakes (e.g., Scott et al., 2018). InSAR analysis has been used to detect local and regional variations in vertical land displacement in areas across the GOM (e.g., Jones et al., 2016; Fiaschi and Wdowinski, 2020) and has been recommended by the NASEM (2018). These results give an insight into the different processes causing ground displacement and how space-based and aerial geodetic data can contribute to quantifying and analyzing these phenomena. Overview

In chapter 1, I used LiDAR differencing between two LiDAR surveys to quantify vertical and horizontal ground displacement relative to the first survey in an area with negligible sediment compaction in south Louisiana, then I compared these estimates with estimates from SAR time series. As an appendix to this chapter, I tested the same LiDAR approach on an area by the coast where sediment compaction and erosion are dominant factors for subsidence. This chapter allows one to see the accuracy of these methods to estimate vertical and horizontal displacements over different settings with slow land motions.

In chapter 2, I use SAR time series to estimate displacement caused by extraction and injection of fluids and compare the results with seismic activity in Northwest Louisiana and East Texas. The goal of this chapter is to investigate whether the earthquakes found between 2019 - 2022 and the injection-extraction of fluids are causing any signal on the surface, this will allow me to complement the information about ground motion in the Haynesville shale for the state of Louisiana caused by these activities.

Finally, for chapter 3, I use SAR time series to estimate seasonal displacements to separate this signal from the long-term motion. These include surface motion due to seasonal hydrological loading and extreme events such as floodings and hurricanes. This chapter is prepared in collaboration with Pritom Sarma from Hebrew University who will develop the modelling approach.

METHODS

- **LiDAR differencing**

LiDAR differencing finds the spatial displacement that occurred between two LiDAR surveys taken at two different times. For this research I use airborne LiDAR datasets. This displacement can be caused by real surface changes that occurred in the period between surveys, by local topographic relief that determines randomness of LiDAR scattering, by misalignments related to flight discrepancies between the surveys, or by the systematic errors during each survey (Scott et al., 2018). Therefore, it is necessary to co-register the point clouds to detect

horizontal displacements and correct the geographical locations and then perform vertical LiDAR differencing between corresponding points.

I did **LiDAR co-registration** using the Iterative Closest Point (ICP) algorithm implemented by Scott et al., (2018) in MATLAB. ICP performs 3D LiDAR differencing by calculating rotations and translations of one survey with respect to the other (Scott et al., 2018; Nissen et. al., 2012). This algorithm uses user-defined core points in each LiDAR point cloud and assumes that each one behaves as a rigid body (Nissen et. al., 2012). ICP iterates as follows: 1) Finds the closest core point in the old point cloud for each core point in the new point cloud, 2) Calculates translation and rotation of each core point in the old point cloud, 3) Iterates until a minimum distance is reached or until a certain number of iterations are completed (Scott et al., 2018; Nissen et. al., 2012). I use ICP in two ways: using LiDAR ground points classified as such by the distributors, and separately using LiDAR points from surfaces that should be stable over time filtering the data with PDAL tools (PDAL, 2018).

After applying horizontal co-registration, I did **vertical differencing** using the Geomorphic Change Detection (GCD) software which detects topographic and volumetric changes using Digital Elevation Models (DEM) (Wheaton et al., 2010). The DEMs were created using the co-registered LiDAR data. The vertical accuracy of the results is given by standard error propagation and depends on the accuracy of the original point clouds (Wheaton, 2018).

- **Interferometry and Time-Series**

InSAR (Interferometric Synthetic Aperture Radar) and InSAR time series are geodetic tools used to measure ground deformation at large spatial scales (Massonet and Feigl, 1998; Osmanoglu et al., 2016). **InSAR** allows one to calculate the phase changes between two radar images taken at different times and almost from the same point of view. The resulting image is an interferogram. It has relative phase changes that represent variations in distance between the ground and the satellite. These describe surface deformation (Massonet and Feigl, 1998). However, an interferogram also records phase contributions from other phenomena such as Earth's curvature, orbital errors, topographic contributions, atmospheric delays, and noise; all these must be removed from the signal to obtain the accurate displacement (Massonet and Feigl, 1998; Xia, 2010). After removing phase errors, it is necessary to unwrap the phase to estimate absolute phase change and geocode the information into a geographic coordinate system (Rosen et al., 2011). Orbital errors and Earth's curvature distortions are corrected using satellite orbits and auxiliary data. This is a minor concern due to the current satellite orbital precision. Topographic contribution is removed using a DEM of the study area. Atmospheric delay is separated into two signals: ionospheric and tropospheric delays (Massonet and Feigl, 1998). Ionospheric corrections are not a major concern for this analysis because I use C-band images which are weakly affected by ionosphere delay (Liang et al., 2019). On the other hand, I must deal with tropospheric delays that depend on pressure, temperature, and water vapor in the troposphere which can vary temporal and spatially (Fattahi and Amelung, 2015). To correct these errors, I use the global weather model Generic Atmospheric Correction Online Service (GACOS) due to its performance and coverage of the study areas (e.g., Murray, et al., 2019).

InSAR time series is a technique that uses many interferograms to create an almost continuous record of displacement for each pixel. There are different algorithms to create InSAR time series, I use SBAS (Small BAseline Subset). SBAS uses a stack of unwrapped

interferograms with small temporal and spatial baselines, these interferograms must be co-registered to the same reference image (Yunjun et al., 2019). This algorithm uses distributed scatterers and takes advantage of redundant stacks, meaning that the pixel's coherence does not have to be that high, which is useful for vegetated areas (Osmanoğlu et al., 2016; Yunjun et al., 2019).

SBAS processing is divided into two steps: 1) Network inversion, where one can discard interferograms with low coherence, select a reference point for the time series, calculate unwrapped errors and finally perform network inversion to minimize the residuals of the time series. 2) Phase corrections include the corrections mentioned above but in this case are applied during the creation of the time series and not directly to the interferograms because is computationally more efficient (Yunjun et al., 2019).

Interferograms and interferometric stacks are created using the ISCE2 (Interferometric synthetic aperture radar Scientific Computing Environment) software which is openly available via GitHub repositories and funded by the NASA-ISRO SAR (NISAR) project (Rosen et al., 2011). This software allows one to incorporate all the mentioned phase corrections and unwrap and geocode the phase to obtain surface displacements in the line of sight. I used MintPy (Miami INsar Time-series software in PYthon) to create the InSAR time series. MintPy receives unwrapped and co-registered stacks from ISCE2 and other packages. It performs the steps described above and is also openly available in GitHub repositories (Yunjun et al., 2019).

- **GNSS time series analysis**

The estimated displacements in the north, east, and up components for the GNSS continuous stations in each study area were estimated by the Nevada Geodetic Laboratory - NGL (Blewitt et al., 2018). For each project, I use one of the stations as a reference point for the LiDAR and/or InSAR time series to tie the results to a ground point with known motion. I considered the length of the station time series (> 5 years) and the coherence value on the InSAR time series (≥ 0.3) to select the reference station. This connection ensures that all the measurements are referred to the same terrestrial reference frame and are comparable with each other (Mahapatra et al., 2018).

The GNSS station was tied to the InSAR time series by projecting to the Line-Of-Sight (LOS) the displacements of the station using the incidence and heading angle for each dataset. For ICP, the tie was done in the three components, and for LiDAR differencing it was done only in the vertical component. Then, I calculated the difference between the displacement of the GNSS station and the results from LiDAR and InSAR in the location of the station. That difference is added/subtracted from each dataset to match the results with the results of the station in its location. Due to this process, the original results are shifted by a constant, but this process does not change the errors. The other stations are used as control points to compare with the results after the connection of the datasets.

CHAPTER 1: Subsidence variations due to human-related activities and relation with Quaternary fault traces in South Louisiana.

• Background and goals

The study area for this project is in East Baton Rouge, Louisiana. This region is characterized by two Quaternary faults (Baton Rouge - BR and Denham Springs - DH) that cut compacted and cemented Pleistocene sediments. Therefore, I can constrain vertical displacement causes to fault movement and anthropogenic activities for the last decades (Fig. 1). I limit the study period between 1999 (RMSE = 15 cm, Point space = 4 m) and 2018 (RMSE = 3.6 cm, Point space = 0.33 m) due to the LiDAR surveys were taken in these years.

Fault slip and creep are difficult to quantify because they can be episodic and slow, and the signal can be masked by faster processes (Gagliano et al., 2003). The relation between fault slip and vertical displacement across the GOM has been quantified in few studies at different temporal and spatial scales with rates ranging between 0.02 – 16.9 mm/y (e.g., Gagliano et al., 2003a, 2003b; Dokka et al., 2006; Shen et al., 2016; Culpepper et al., 2019a; Hopkins et al., 2021). Some faults or fault segments across the GOM seem to be reactivated by human activities, and then as consequence, there has been subsidence (e.g., Morton et al., 2002; Dokka, 2011). Other faults have shown small throw rates over geological time scales implying that fault slip is not a significant process causing subsidence (e.g., Shen et al., 2017). Some studies, however, show faster rates in the shorter and recent temporal scales (Hopkins et al., 2021). On the other hand, extraction and injection of fluids are processes that can cause large vertical ground displacement in localities near the wells (e.g., Jones et al., 2016; Shirzaei et al., 2016). Extraction of fluids can reduce the pore pressure and cause permanent reservoir compaction leading to subsidence (Puskas et al., 2017), while injection can increase pore pressure which can cause uplifting, this has triggered seismic activity in some areas on the GOM (e.g., Shirzaei et al., 2016).

The aquifer system in Baton Rouge is part of the Southern Hills Aquifer (SHA) and the Mississippi River Alluvial Aquifer (MRAA) (Tomaszewski et al., 2002). SHA is composed of interbedded layers of compressed clay/silt and porous sand (Tomaszewski et al., 2002). The sands form ten independent aquifers organized vertically and named after their depth under the Industrial District (Tomaszewski et al., 2002). Aquifers in the northern block of the Baton Rouge fault recharge from infiltration in areas north of the DS fault (e.g., Vahdat-Aboueshagh and Tsai, 2021), meaning that the DS fault is permeable and allows flow towards the main District (Elshall et al. 2013). Large volumes of groundwater removal have affected reservoirs in the Baton Rouge area forming cones of depression at local and regional scales (White, 2017; Chen et al., 2023), and saline water from southern areas has intruded into some of these sands (Nasreen, 2003; Elshall et al., 2013). The BR fault plays an important role in the aquifers' dynamics in Baton Rouge; it is a barrier for saline water coming from the southern area, but it may serve as a conduit that can allow lateral intrusions due pressure changes caused by high pumping of groundwater at the north of the fault (e.g., Anderson et al., 2013; Chen et al., 2023).

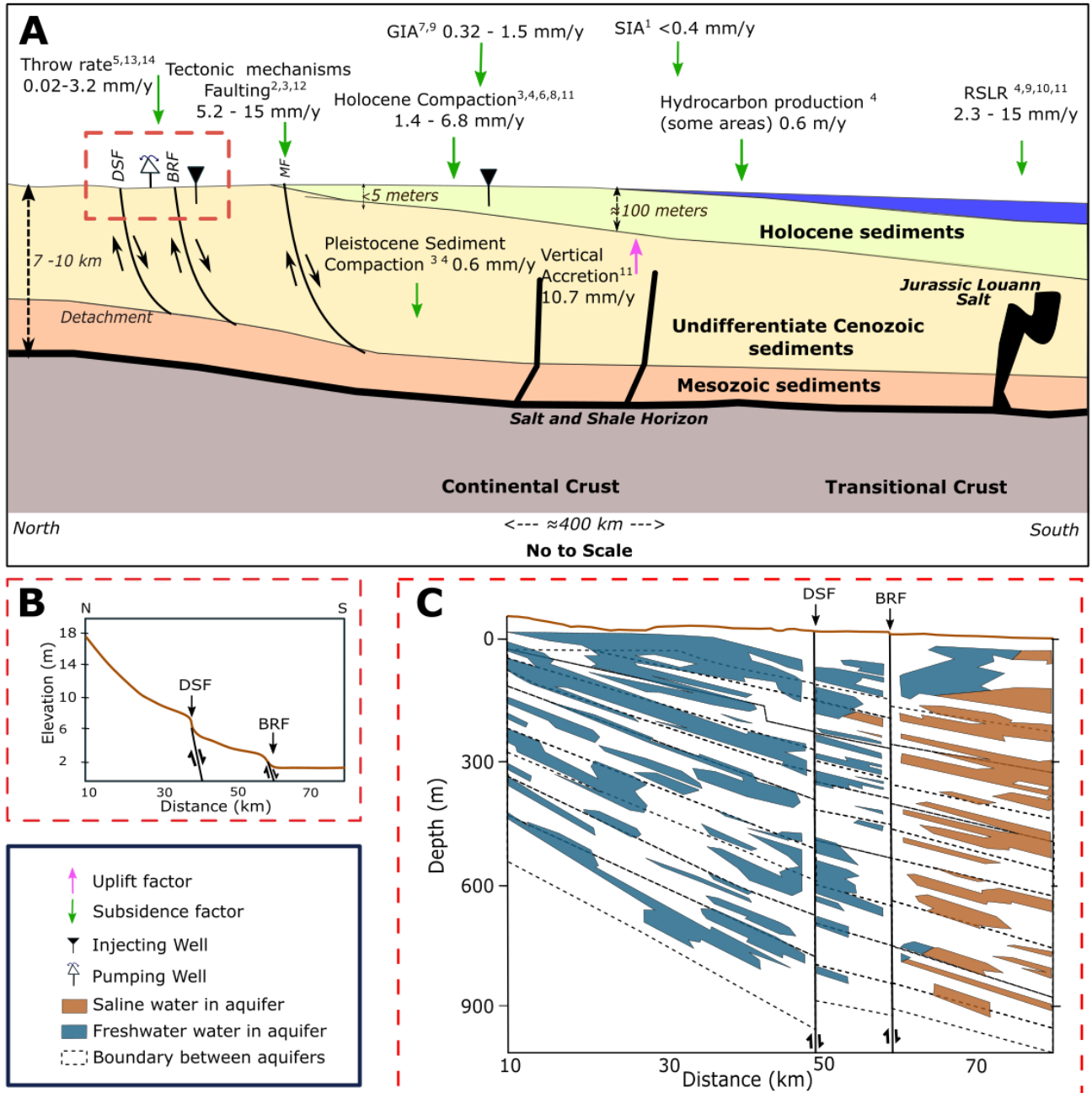


Figure 1: A) Schematic model of the extensional-contractional complex in southern Louisiana. Faults included in the figure: Baton Rouge Fault (BRF), Denham Springs Fault (DSF), Golden Meadow Fault Zone (GMFZ), Michoud Fault (MF). Study area enclosed in red rectangle. Modified from Shen et al. (2016). B) Topographic profile of the study area. Modified from Gasparini et al., (2015). C) Hydrogeological setting under the study area enclosed in (A). Aquifer boundaries are an approximation for the lithologic, hydrogeologic, and aquifer system contacts. The top one is the 400-ft sand and the bottom one is the 2800-ft sand. After White (2017). Subsidence and uplift rates from: Kuchar et al. (2018)¹, Dokka et al. (2006)², Dokka, (2006)³, Chan et al. (2007)⁴, Shen et al. (2016)⁵, Keogh and Törnqvist (2019)⁶, Love et al. (2016)⁷, Karegar et al. (2020)⁸, Karegar et al. (2017)⁹, Penland and Ramsey (1990)¹⁰, Jankowski et al. (2017)¹¹, Jones et al. (2016)¹², Penland et al. (2001)¹³, Hopkins et al. (2021)¹⁴.

For this analysis, I only used active wells extracting or injecting fluids between 1999-2020 and were on the database of the Louisiana Department of Natural Resources website by August

2021. However, wells that operated before can, in some cases, cause delayed pore pressure changes and deform the surface (e.g., Shirzaei et al., 2016).

The purpose of this research is to quantify recent vertical and horizontal surface displacement using LiDAR data taking advantage of its high spatial resolution in an area that is almost unaffected by sediment compaction and that is highly urbanized. The results of this research allow us to know 1) whether the BR and DS faults are causing vertical land motion by fault slip measurable with this dataset, 2) whether the measured vertical surface motion is correlated with fluid extraction/injection or urban development. I validated these estimates with results from InSAR time series (chapter 3 - paper) and motion estimates from GNSS continuous stations in the study area. I assumed a modern fault creep of ~3 mm/y from Hopkins et al. (2021).

• Data and Methods

The area is covered by two LiDAR surveys spanning 19 years, both surveys cover the portion of the TBRZ fault located in the East Baton Rouge Parish in southern Louisiana. The first dataset was collected in March of 1999 and has a point space of 4 m, a pulse rate of 15 kHz, and a vertical accuracy measured as the Root Mean Square Error (RMSE) of 15 cm (USACE, 2001). The newest was collected between March and April of 2018, has a point space of 0.33 m, a pulse rate of 450 kHz, and a vertical accuracy of RMSE=3.6 cm (USGS, 2019).

To perform LiDAR differencing Ico-registered the surveys using ICP using a window size of 50 meters to co-register ground points and stable surface points separately. In both cases, approximately 122,400 core points were created. The results of each core represent the displacement of a window. These results were filtered to have only displacements between 0 to 1 m to eliminate outliers showing artifacts (e.g., new constructions), and not natural displacements. Then, the results were averaged to have a representative point per 2.25 km². The averaged results were evaluated using a margin of error metric with a 95% confidence interval. Using the co-registered data, I applied vertical differencing using the GCD software and a DEM for each survey, both DEMs have a pixel size of 5 meters. There are two GNSS continuous stations in the study area (1LSU and SJB1), both are south of the BR fault. I use the 1LSU GNSS station to tie the results to a known ground point. The SJB1 station is used to compare the results from all the methods.

• Main Results and Conclusion

For the case of discussion, I call the footwall block of the BR fault the northern block and the hanging wall of the BR fault the southern block (Fig. 2C). LiDAR vertical difference and ICP show similar results regarding vertical displacement; there is subsidence across the entire study area with larger displacement in the northern block, while the southern block has areas of uplift.

ICP using LiDAR ground points (Fig. 2A) indicates that the uplift region on the southern block is small while the northern block experience greater subsidence. ICP using LiDAR stable points (Fig. 2B) shows that uplifted area is wider than in the southern block. Results from ICP using stable points and ground points have similar outcomes, though results from stable points have larger errors than those from ground points, probably because there are fewer stable

surfaces in 1999 compared to ones found in 2018. Due to the lack of stable surfaces many core points are discarded as outliers. ICP results show that subsidence increases from southwest to northeast (Fig. 2C and 2D). LiDAR vertical differencing results show displacement in a more detailed resolution, this enables to detect some areas of interest with larger values of displacement (Fig. 3).

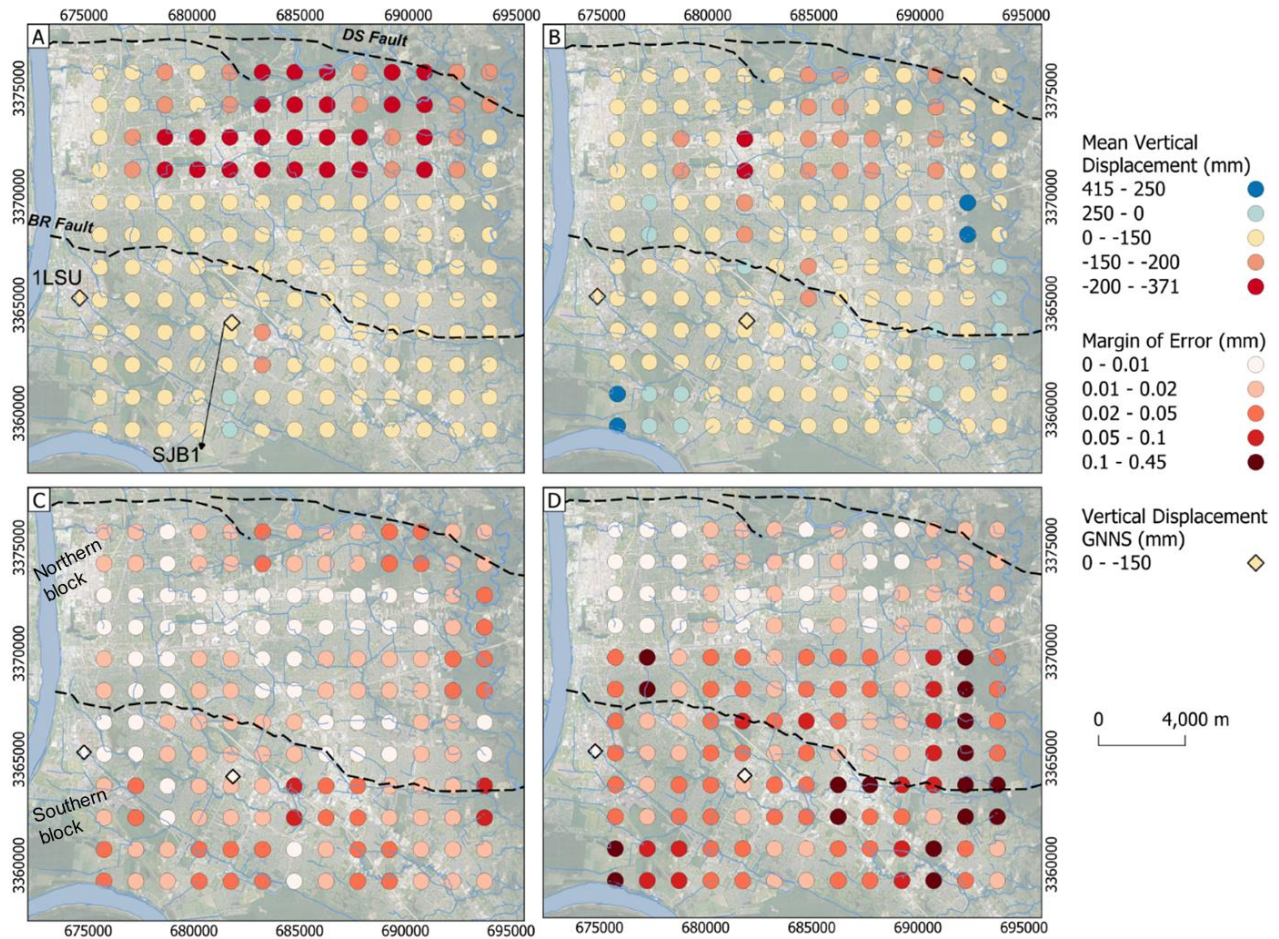


Figure 2: Vertical displacement calculated from ICP algorithm. (A) Mean displacement using LiDAR ground points. (B) Mean displacement using stable surfaces LiDAR points. (C) Margin of error of the results for (A). (D) Margin of error of the results for (B). Each circle in A and B represents the mean displacement of an area of 2.25 km². Errors in C and D are calculated as the margin of error with respect to the mean. Rhombus are the vertical displacement calculated using rate from the GNSS CORS stations for 19 years. Base map imagery from QuickMapServices - QGIS (Map data ©2015 Google)

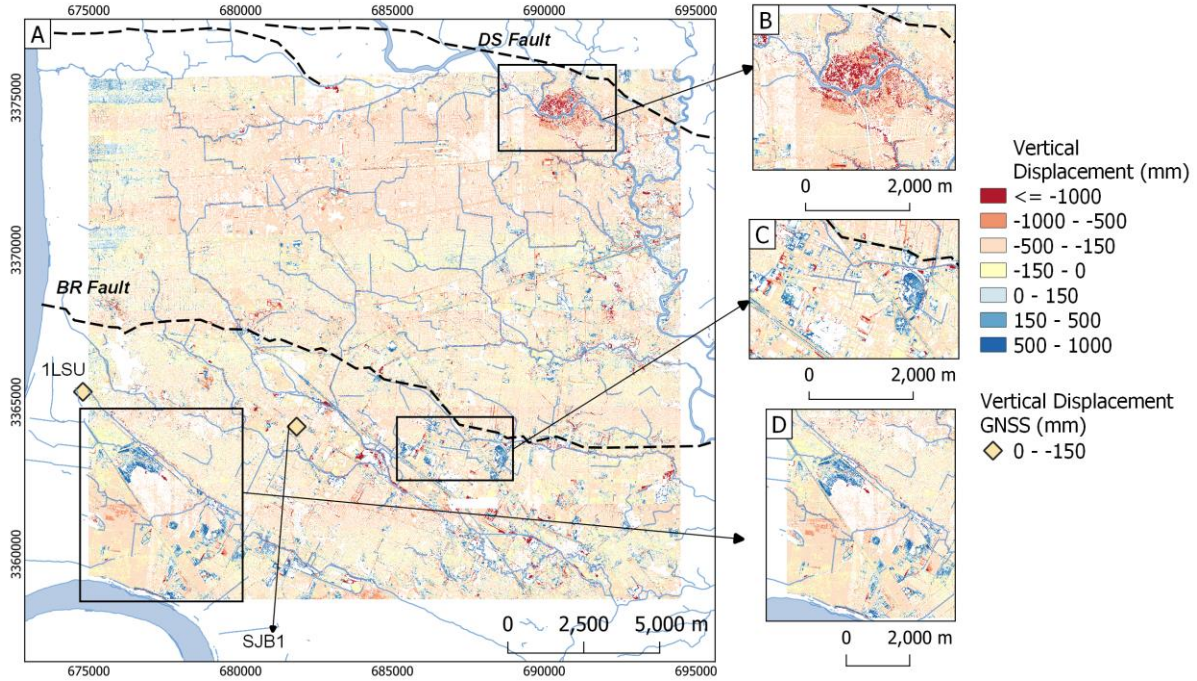


Figure 3: Vertical displacements calculated from Vertical DEM differencing. (A) Vertical displacements calculated the co-registered DEM using results from ground points. (B, C, D) Some areas of interest discussed in the text.

ICP results show that the entire area moved to the east direction between the two surveys (Fig. 4). Horizontal displacement calculated with LiDAR ground points is more homogenous in the whole area (Fig. 4A). Results using LiDAR stable points (Fig. 4B) have a slightly different behavior for each block; the northern block moved mostly to the east direction but the area near the east segment of the BR fault shows north-east motion. The southern block has more variation but the motion towards to north is larger than the results in the northern block.

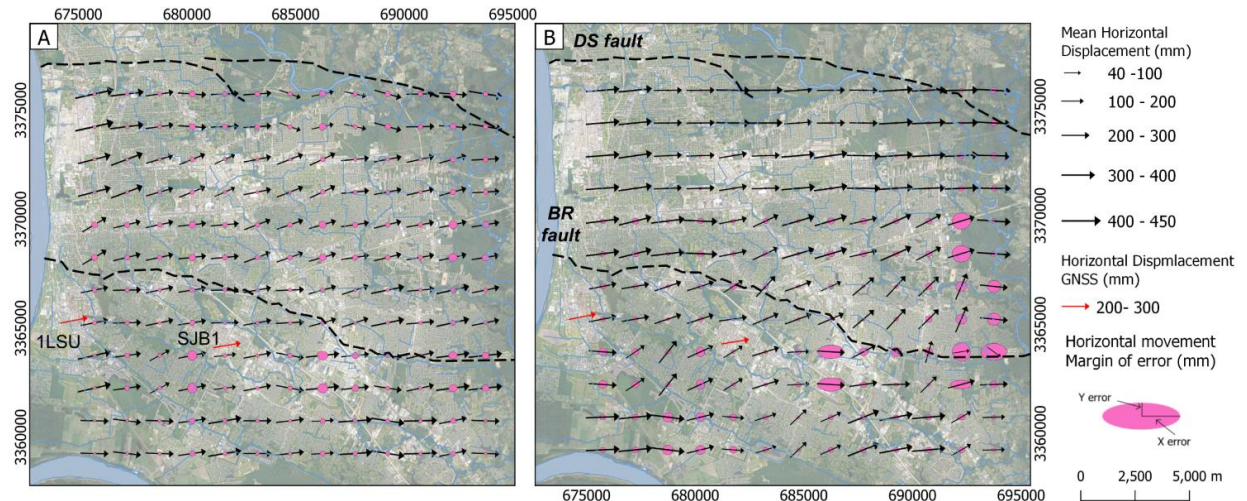


Figure 4: Horizontal displacements calculated with the ICP algorithm. (A) Horizontal displacements using ground LiDAR points. (B) Horizontal displacements using stable surface LiDAR points. Each black arrow represents the average displacement of an area of 2.25 km². Arrow directions represent the mean displacement direction, and the length of the arrow represents the mean displacement magnitude. Ellipses show the error multiplied by 30 for visualization, where X-error represents the error in

the east component and Y-error represents the error in the north component. Red arrows are horizontal displacements using the rates from the GNSS stations for 19 years. Base map imagery from QuickMapServices - QGIS (Map data ©2015 Google).

Summary of the results per block and per method are presented in Table 1.

Table 1: Main statistics per block for each tool. MOE stands for Margin of Error. Numbers market with * refer to values derived from the estimates. These numbers do not have an estimated error and are for comparison purposes. All the values are in NAD83.

PSI (LOS direction)						
Dataset	Time Span	Block	Mean velocity (mm/y)	Median velocity (mm/y)	MOE of the mean velocity (mm/y)	Mean displacement (mm)
EnviSAT	2004-2010	Northern	-10.869	-11.225	0.0384	-65.214*
		Southern	-8.030	-7.839	0.0614	-48.181*
Sentinel-1	2017-2020	Northern	-13.65	-13.645	0.00471	-40.96*
		Southern	-10.559	-10.82	0.00895	-31.68*
ICP						
Dataset	Direction	Block	Mean velocity (mm/y)	Mean displacement (mm)	Median displacement (mm)	MOE of the mean displacement (mm)
Ground point cloud	Up	Northern	-8.385*	-159.313	-140.9	13.8
	North		2.51*	47.66	49.54	9.26
	East		13.964*	265.31	269.41	10.32
	Up	Southern	-5.124*	-97.352	-101.4	8.03
	North		1.162*	22.072	27.04	8.45
	East		13.845*	263.05	259.41	10.72
Stable point cloud	Up	Northern	-5.023*	-95.433	-117.89	19.671
	North		2.52*	47.866	25.04	13.155
	East		14.44*	274.389	295.9	15.638
	Up	Southern	-2.391*	-45.422	-82.89	28.75
	North		2.845*	54.056	56.04	12.192
	East		11.89*	225.9	225.9	19.595
DEM differencing						
Dataset	Direction	Block	Mean velocity (mm/y)	Mean displacement (mm)	Median displacement (mm/y)	MOE of the mean displacement (mm/y)
DEM's from Ground point clouds	Up	Northern	-11.15*	-211.859	-207.565	0.00014
	Up	Southern	-7.005*	-133.09	-167.9	0.00025

GNSS				
Station	Direction	Block	Mean velocity (mm/y)	Mean displacement (mm)
1LSU	Up	Southern	-4.31	-81.89*
	North		2.66	50.54*
	East		13.39	254.41*
	LOS EnviSAT		-9.81	-58.86* (2004-2010)
	LOS Sentinel		-10.89	-32.6* (2017-2020)
SJB1	Up	Southern	-1.35	-25.65*
	North		2.22	42.18*
	East		13.69	260.11*
	LOS EnviSAT		-7.23	-43.38* (2004-2010)
	LOS Sentinel		-8.4	-25.2* (2017-2020)

I compared the LiDAR results with InSAR time series processed with PSI and continuous GNSS stations in the area, average values can be found in Table 1. LiDAR results indicate that the northern block is subsiding faster than the southern block with respect to the 1LSU GNSS station. The InSAR time series also indicates that the northern block is moving away from the satellite faster than the southern block in the Line of Sign direction. InSAR measurements indicate that the BRF serves as a boundary between the areas of rapid and slow subsidence. This behavior contradicts the long-term displacement of the down-to-south normal fault. In the southern block, there are two GNSS stations. I used the 1LSU station to tie the results and SJB1 for comparison. These stations show that the southern block is subsiding and moving horizontally towards the E-NE direction. This motion agrees with the direction of the ICP results. SJB1's magnitude is better replicated by the results with stable LiDAR points (Fig. 2 and Table 1).

During the study period, 592 wells actively extracted water mainly for industrial and public supply uses. Most wells are in the northern block and are at deeper depths than in the southern block. Recent groundwater models show that there is a cone of depression between the DS and the BR faults (e.g., Chen et al., 2023). These results (LiDAR and InSAR time series) support the hypothesis that the northern block is part of a regional depression cone caused by water extraction in the city limited by the faults (Fig. 2 and 3). The relationship between groundwater withdrawal and subsidence is known and supported by several studies globally and in the GOM (e.g., Guzy and Malinowska, 2020; Fiashi and Wdowski, 2020). On the other hand, the areas with the slowest subsidence are in the southern block (Fig. 3C and 3D), these areas have most of the injection and oil/gas wells in the area. Multiple studies have shown that injection of fluids can increase pore pressure at depth which can diffuse and cause local uplift (e.g., Anderson et al., 2013; Shirzaei et al., 2016). Then, an increase in subsurface pressure caused by injection can be an explanation for the slower displacements and rates in the southern block. Comparison with the LiDAR and InSAR results with the depth and injected volume

indicate that shallower wells may create a signal, although the signal of wells located in the area 3D cannot be detangled.

This study shows how LiDAR data can be used to estimate vertical and horizontal displacements in areas with slow motions for the first time. These results were confirmed with other geodetic tools (InSAR and GNSS), all present similar results in terms of magnitude and direction of the motion for the Baton Rouge area. Although it is important to highlight that uncertainty of LiDAR results is limited by the number of surveys, the systematic error of each survey, the structures on the study areas, and the different processes that can be affecting the area. The annex in this document present an example of a test area where LiDAR methods likely are not a good approach even with good space resolution of both surveys.

CHAPTER 2: Ground vertical displacement and its relationship with injection and extraction of fluids in North Louisiana.

- **Background and goals**

The study area for this project is on the border of East Texas and North Louisiana where the Haynesville and Bossier shale plays are located (Fig. 5A). This area is of particular interest because the Haynesville and Bossier plays are organic-rich mudrocks with the capacity of producing trillions of cubic feet of gas (Hammes and Frebourg, 2012). This positions it as one of the most productive shales gas basins in the country (Speight, 2020). The Haynesville and Bossier shales are often recognized as one formation with depths between 3000 - 4700 meters with an area of ~23,000 km² that formed ~136 million years ago (Hammes et al., 2011; Speight, 2020). However, these two shales are distinguished by the amount of clay deposited in each shale. The Haynesville shale which is at the bottom has less clay than the Bossier shale which is on top (Hammes and Frebourg, 2012). Up until 2001, the faults in North Louisiana were inactive (Stevenson and McCulloh, 2001).

During the last decades, the USA has become one of the main producers of natural gas thanks to the development of horizontal drilling and hydraulic fracturing technologies to produce from tight formations such as the Haynesville and Bossier shale plays (Speight, 2020). Due to the depth and high temperatures that range between 125-195°C in the Haynesville shale, it is necessary to use hydraulic fracturing to keep production (Speight, 2020). Extracting activities in the shale started in 2008 and they continue nowadays (Durham, 2008).

Hydraulic fracturing has been related to different hazards such as water consumption, groundwater contamination, surface chemical spills, emission of toxic gases, and induced seismicity in different parts of the country (e.g., Jackson et al., 2015). Induced seismicity due to activities related to fluid injection (hydraulic fracturing, enhanced oil recovery (EOR), and wastewater injection) has been investigated in multiple papers (e.g., Ellsworth, 2013; Rubinstein and Mahani, 2015). Injection-induced seismicity can be caused by different mechanisms that change the stress conditions on nearby faults. These mechanisms include increasing pore pressure on the fault, thermoelastic deformation when injecting cold fluids in warm formations, changing the fault-load conditions, or aseismic slip caused by pore pressure (Rubinstein and Mahani, 2015; Eyre et al., 2019). Most of the injection-induced earthquakes in the country are

caused by wastewater injection and just a portion by hydraulic fracturing. In Canada, however, hydraulic fracturing is the main reason for injection-induced earthquakes (Ellsworth, 2013; Rubinstein and Mahani, 2015). Weingarten et al. (2015) estimate that 60% of the induced seismicity in Mid-USA has been caused by wastewater injection since 2009, however before 2000 this percentage was <20%. They argue that injection of wastewater may be more prompt to cause seismic activity than EOR because, for the last one, operators need to balance reservoir pressures to maintain production.

There is debate about which operation parameters influence the probability of injection-induced seismicity. Injection rate appears to be one of the most important parameters; rates of >48,000 m³/month are most likely to produce an earthquake (e.g., Weingarten et al. 2015). However, this same study acknowledges that due to lack of information about pore pressure in the reservoir before injection and lack constant monitoring of the bottomhole pressure during injection, these variables cannot be discarded (Weingarten et al. 2015).

Information from the Department of Natural Resources of Louisiana indicates that there are 3903 active wells producing gas from the Haynesville shale with depths ranging between 2743 and 9144 m. There are 589 active injection wells just in the shale area in Louisiana with depths ranging between 0 and 5234 meters (SONRIS, 2023; Fig. 1). There are 1973 active injection wells in Louisiana in the study area and not on top of the shale with depths ranging between 0 and 3940 meters. The Texas Railroad Commission (TRC) reports 12657 wells extracting gas from the shale and there are 220 injection wells in the shale. There are 326 injection wells in the area outside the shale. It is important to consider the available information about the injection wells outside the shale because in some cases, induced earthquakes can occur far from the injection well and at deeper depths (Rubinstein and Mahani, 2015).

The study area is characterized by low seismic activity. However multiple researchers have described events in the study area (Fig. 5); one of the first reports occurred in 1964 during the construction and maintenance on the Toledo Bend and the San Rayburn dams, in this case there are reports of ~70 microseisms between April and August of that year (Henley, 1965). Twenty-five of the events had a magnitude between 2 – 4.4 and were compiled by Stevenson and McCulloh, (2001) (Fig. 5C). Microseismicity after water impoundment at dams is not unusual – (e.g., Ellsworth, 2013). Owing to the absence of seismic monitoring equipment, little is known until USARRAY was deployed in the Central U.S in 2008-2013. The next set of events occurred between 2008 and 2013 as documented in several studies. First, Frohlich et al., (2014) compiled 65 events between 2008-2013 with magnitudes ranging between 0.5 - 4.8 and depths between 1.68 - 4.62 km. In this study they conclude that the events after the main event (May, 17 2012) occurred along a linear feature that coincides with mapped basement fault and within an area of ~3 km of four injection wells with injection rates between 8,000-43,000 m³/month (Fig. 5D). Next, Walter et al., (2016) complemented the previous set of earthquakes. They found more earthquakes between 2010 and 2012 in Timpson, and other clusters in Bienville, LA, and in the border area. They suggest that the earthquakes were also caused by injection, and in the Bienville area gas extraction with hydraulic fracturing also may have played a role (Fig. 5E).

The largest event recorded in the area with a magnitude of 4.8 and a depth of 4.5 km happened on May 17, 2012. This earthquake and aftershocks caused superficial damage to some properties (Frohlich et al., 2014; Fig. 5A). Shirzaei et al., (2016) used InSAR time series to estimate how much uplift and volume changes accompanied this earthquake. They conclude that in the area with most uplift (>3 mm/y) are two wells injecting at moderate injection rates ($\sim 28,600$ m³/month) and shallow and at depths (~ 850 m), while the area on top of the earthquake epicenter has two wells that injected at higher rates ($46,800$ - $71,550$ m³/month) and deeper depths (~ 1850 m).

The most recent investigation found earthquakes with magnitudes varying between 0.7 to 3.2 with depths between 0.01- 13 km in the area (Ebinger et al., 2022 – ISLA report; Fig. 5A). *The purpose of this research is to determine whether there is ground deformation detectable with InSAR time series caused by the injection of fluids near the areas of the seismic events found during the ISLA project. The results of this research will allow us to know: 1) Whether injection of fluids is related to deformation across the region, and 2) if there is deformation, we will know whether it is occurring as uplift or as slip along stable faults nearby.* Shirzaei et al., (2016) demonstrated how ground deformation and earthquakes occur in the area where different injection rates and injection depth seem to play an important role.

• Data and Methods

The study area is covered by information collected by Sentinel-1 data collected between September 2016 and September 2022. Sentinel-1 captures data on the C-band and in the Interferometric Wide mode (ESA, 2021). Due to the area size, the dataset is divided into two parts; the first part of the dataset covers most of the area in Louisiana and was captured in the relative orbit 63. It is subdivided into north and south. The second part covers the study area in Texas and was captured in the relative orbit 136, also subdivided into north and south. The dataset has one image per month for each subdivision for a total of 292 Sentinel-1 images. I created the InSAR time series using SBAS.

The study area is highly vegetated, therefore, it is likely that coherence is affected by temporal decorrelation in most of the area (Osmanoğlu et al., 2016). To know how decorrelation affects the results I processed each InSAR time series two times, each time with a different reference point. This approach allows me to confirm the direction motion of the points that are far from each of the reference points. Motion of areas far from the reference point have largest uncertainties than areas near the reference point (Crosetto et al., 2016). In all cases the reference point was placed in the location of a GNSS station with known coordinates and displacement (Fig. 6).

There are 47 GNSS stations in the study area (23 in Texas, 23 in Louisiana, and one in Arkansas). Velocity and displacement time series are obtained from NGL (Blewitt et al., 2018). The GNSS velocities are projected to the LOS direction to compare with the InSAR time series from Sentinel-1. Some GNSS stations are used as reference points in the InSAR time series, and all the dataset is used to remove rigid plate motion from the InSAR time series which can appear as a ramp on the results (Stephenson et al., 2022; Fig. 6A and 6B).

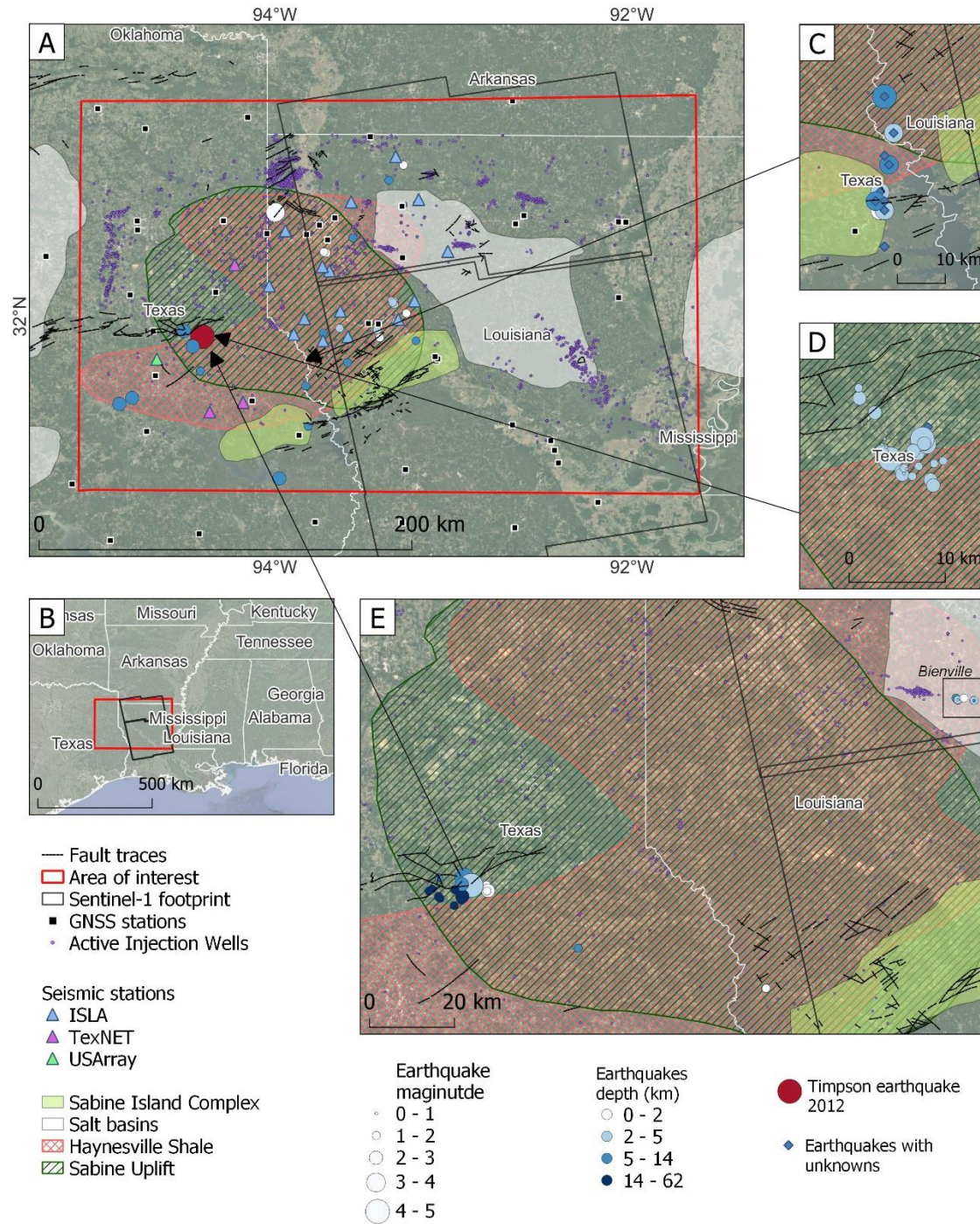


Figure 5: A) Location, geological and seismologic context for the study area. Recent earthquakes detected during the ISLA project between July/2019 and January/2022 (Ebinger, et al., 2022) and Shirzaei et al. (2016), with the seismic equipment used for the analysis, injection wells from SONRIS (n.d.) and TRC (n.d.), faults from Wheeler et al., (1998), Structural elements from Hammes et al., (2011), GNSS information from Nevada Geodetic Laboratory GPS Networks Map (Blewitt et al., 2018), UNAVCO, (2006)), last access on February 23, 2023. B) Inset showing the location of the area with respect to the Gulf of Mexico. C) Earthquakes occurred between April and August from 1964 (Henley, 1965; Stevenson and McCulloh, 2001). D) Earthquakes occurred between April/2008 and May/2013 (Frohlich et al., 2014; Shirzaei et al., 2016). E) Earthquakes occurred between April/2010 and July/2012 (Walter et al., 2016). Earthquakes without information about epicenter depth and/or magnitude are presented as a blue rhombus.

- **Preliminary work**

I am presenting the results for the stacks of the relative orbit 63 and the GNSS stations in northern Louisiana (Fig. 6). First, most of the area has forest or farmland, due to the large decorrelation caused by vegetation there are not results in these areas. In areas with detectable signals, the InSAR time series in the northern area indicates that the easternmost areas are subsiding in the LOS direction regardless of the reference point location. There are no hydraulic fracturing activities in the area and there are not many injection points, however, conventional extraction of resources and both surface and groundwater pumping may be occurring nearby (Fig. 6A and 6B). Whereas the western area, on top of the Haynesville shale, seems to move more slowly or in some cases towards the LOS direction (Fig. 6A and 6B). The area south of the Haynesville shale (Fig. 6C) seems to be moving far from the satellite more rapidly. In this case the complementary time series (Fig. 6D) lost coherence rapidly and cannot help to understand whether this motion is real or not.

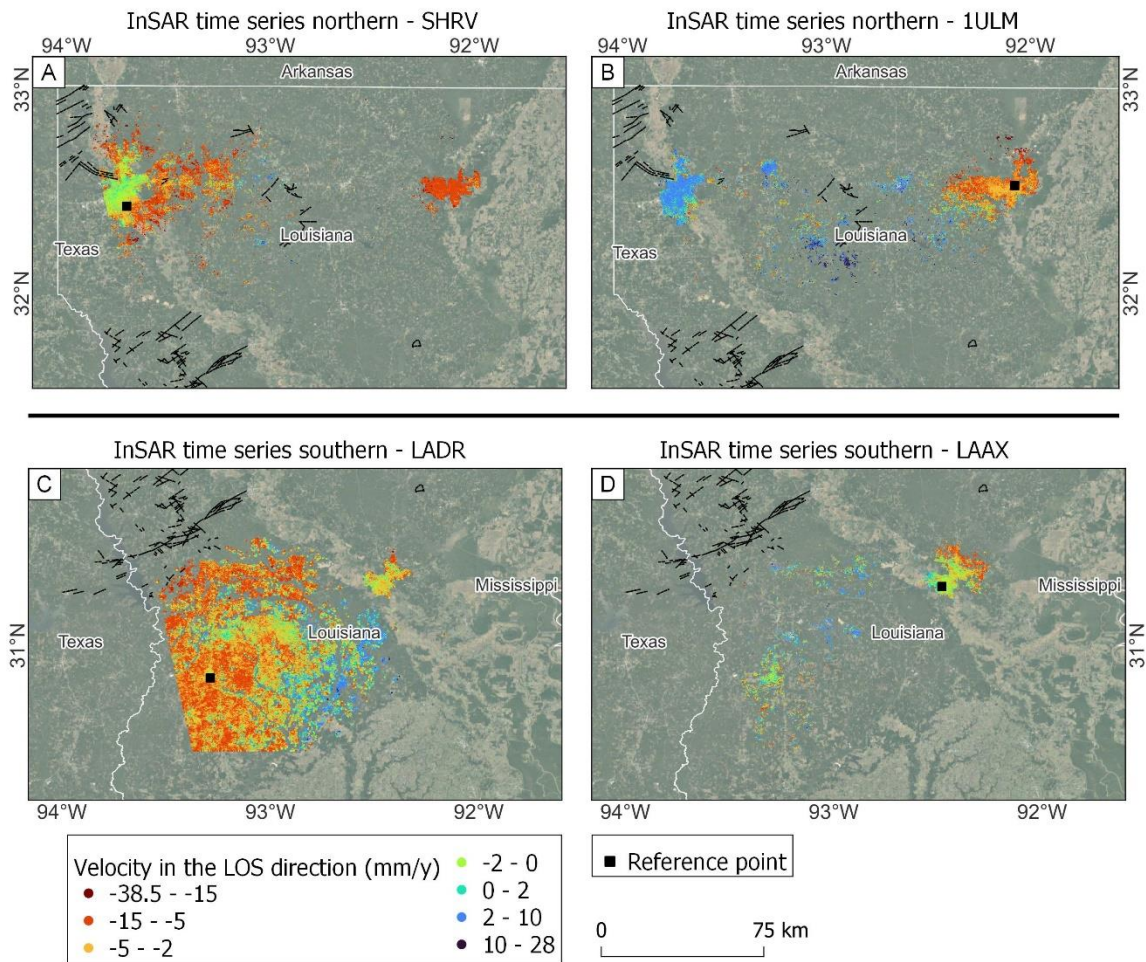


Figure 6: InSAR velocities in the LOS direction. Each time series uses a different reference point, the GNSS station name used as reference point is labeled on top of each panel. All the time series are corrected for plate motion using the GNSS information from NGL (Blewitt et al., 2018). The reference point motion was removed from each time series. Color scale for GNSS velocities and InSAR time series (Fig. 8) is the same.

The results from GNSS indicate that most of the study area is moving away from the satellite at rates between 0 to -5 mm/y. The stations in the northernmost area, however, have positive rates which may indicate uplift (Fig. 7B). The GNSS results are helpful to know how the vegetated areas move where InSAR time series do not produce results. The agreement between these methods can be better observed by zooming in on the areas where there is more confidence about the results, meaning near the reference points. For instance, in Figure 8 centered in the GNSS station SHRV, the rates from GNSS are very similar to the ones estimated from InSAR time series in the north and northwest; they differ by <0.3 mm/y. It is also noteworthy that there are more injection wells in the north where the rates are slower, whereas there are more hydraulic fracturing wells in the south where the rates are faster and show motion away from the satellite. This could be a similar case to the uplift found by Shirzaei et al., (2016). There are also two earthquakes found by Ebinger et al., (2022) with magnitudes of 1.4 and 1.7 at very shallow depths in the south.

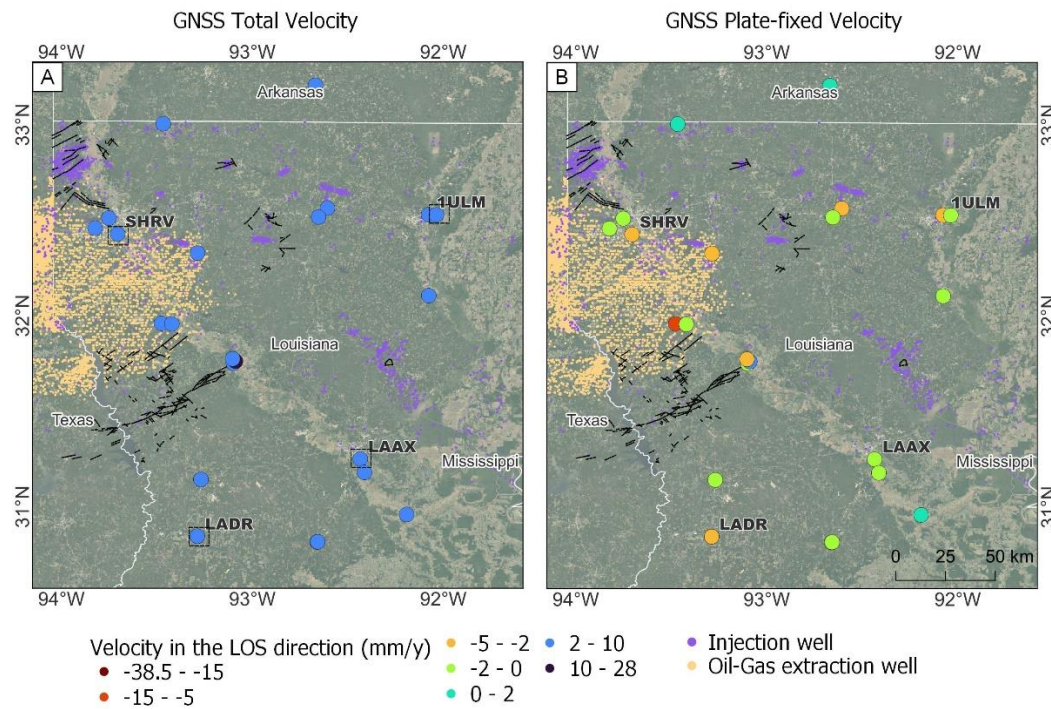


Figure 7: GNSS velocities in the LOS direction. A) GNSS total velocity estimated by NGL (Blewitt et al., 2018), B) GNSS velocity with fixed plate tectonic (North America plate) estimated by NGL (Blewitt et al., 2018). The difference between these two datasets is the motion of the plate which was removed from the InSAR time series in Figure 6. Color scale for GNSS velocities and InSAR time series (Fig. 6 and 7) is the same.

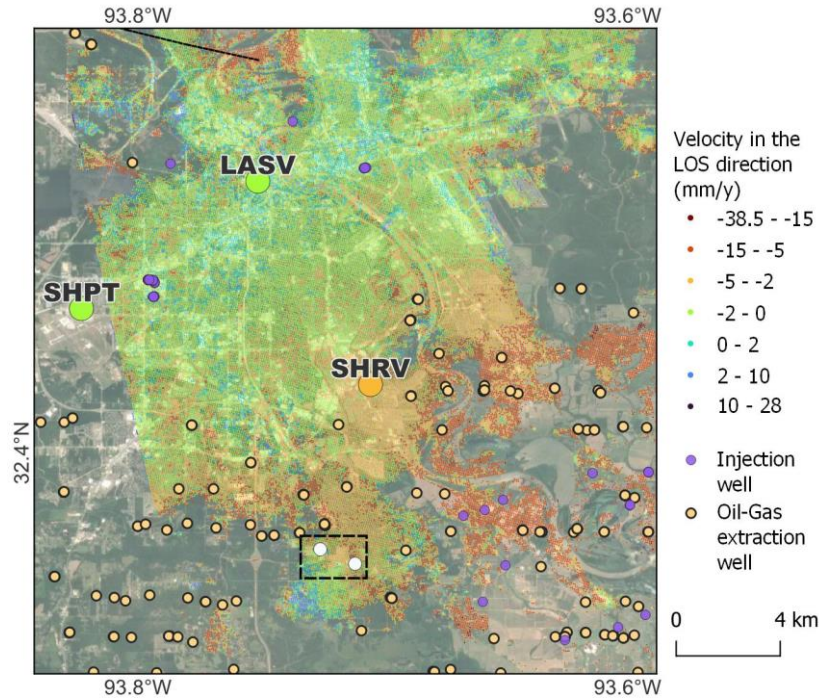


Figure 8: Example of agreement between GNSS and InSAR time series. Injection wells in purple and Hydraulic fracturing wells in dark yellow. Earthquakes with magnitude 1.4 and 1.7 with depths <0.5 km from Ebinger, et al., (2022) in dashed box. InSAR and GNSS results are in the LOS direction and use the same color scale. GNSS stations are the bigger circles with labels.

- **Pending Work**

These are the pending task to complete this project: 1) Process InSAR time series for the Texas area, 2) Compile and compare with injected volumes, rates, and pressure for the wells with this information, 3) Determine whether the most recent earthquakes and injection/extraction activities are related and causing ground deformation, this will be possible after completion of tasks 1 and 2.

CHAPTER 3: Quantifying Hydrological Seasonal Loading of faults with Interferometry in South Louisiana.

- **Background and goals**

The study area for this project is the area of Baton Rouge (same area as Chapter 1; Fig. 1). *The goal of this project is to estimate the mean seasonal signal from hydrological seasonal loading and extreme events such as storms to constrain seasonal forcing models. The results of this work will be part of a collaborative work where we estimate the seasonal forcing and injection-induced subsidence in the area.*

Seasonal ground deformation measured with geodetic data is a field under research mainly due to two different processes that dominate the signal: hydrological loading and poroelastic deformation caused by extraction and recharge of fluids in the aquifers (Kang and Knight, 2023). Hydrological loading refers to the elastic deformation of the crust caused by water loads on or near the surface. These loads mainly affect the vertical component but may cause small horizontal changes (Materna et al., 2021). Poroelastic deformation is caused by

changes in the water head in aquifers. When the pore spaces are filled with water, pore pressure increases inside the rock (Materna et al., 2021; Kang and Knight, 2023). These processes correlate with seasons, but they have an opposite behavior: a water load can cause bending of the crust and there is subsidence, and when the load is removed, for instance by evapotranspiration, there is a rebound and uplift (White et al., 2022). However, water loads occur mostly due to storms and water accumulation during wet periods. During these periods water head rises and causes uplift and during dry periods it falls and causes subsidence (Kang and Knight, 2023). Another factor to consider when estimating seasonal signals from geodetic methods is water withdrawal and injection (e.g., Kang and Knight, 2023).

Some studies have used measurements from InSAR and GNSS to estimate ground deformation caused by water head changes, and then characterize aquifer-system properties (e.g., Chaussard et al., 2014; Neely et al., 2021). They state that the estimated ground deformation and independent hydrological datasets such as water head changes are related. On the other hand, some studies investigate loading using the InSAR and GNSS signals. For instance, after Hurricane Harvey in Texas in 2017, numerous studies have estimated the weight of the accumulated water, the time that took for the crust to be restored to its original elevation, ground deformation, and spatial extent of the deformations using GNSS, InSAR time series, GRACE and independent hydrological datasets (e.g., Milliner, et al., 2018; Miller and Shirzaei 2019). Loading signals from GNSS have also been separated from tectonic signals to estimate hydrological properties in south-east Asia (e.g., Materna et al., 2021). Kang and Knight (2023) indicate that hydrological loading and poroelastic deformation should be separated in the deformation signals measured with InSAR time series. They found that ~56% of the seasonal signal is caused by hydrological loading. Therefore, without any correction poroelastic response can be underestimated by 50-60% on areas where water head has large variations.

Aquifers in the northern block of the Baton Rouge fault recharge from infiltration in areas north of the DS fault on Mississippi and from runoff (e.g., Vahdat-Aboueshagh and Tsai, 2021), meaning that the DS fault is permeable and allows flow towards the area between the faults (Elshall et al. 2013). As mentioned before, this area has been largely affected by groundwater removal where cones of depression have formed (White, 2017; Chen et al., 2023). East Baton Rouge has also been under large hydrological loads, for instance the 2016 Severe Storms and Flooding event (Carney et al., n.d.). This storm produced ~7 trillion gallons of rainwater in south Louisiana affecting mostly the parishes of East Baton Rouge, Livingston, and St. Helena near the Amite and Comite Rivers (Carney et al., n.d.). The National Oceanic and Atmospheric Administration (NOAA) recorded other four flash floodings in the area during the study period.

There is ongoing investigation on the seasonal deformation caused by hydrological loads on the coast of Louisiana. Schuler and Luttrell (2022) use continuous GNSS stations to estimate long-term subsidence and seasonal signals from hydrological loadings, specifically the Mississippi River and large water bodies, between 2016-2020. They concluded that the amplitude of seasonal loading is 20-25 mm/y, however, they do not separate the loading sources or other possible seasonal processes.

- **Data and Methods**

I used Sentinel-1 data collected between January 2016 and August 2022; all the images belong to the relative orbit 165. The dataset contains one image per month for a total of 74 images (images not included February and June 2016, June 2020, and July and August 2022), all the images were captured at the end of the month after the 20th day. I created an InSAR time series using SBAS with the SJB1 GNSS station as the reference point (Fig. 9). The study area is highly urbanized and has <600 km², so decorrelation is not a big problem in this case. The area only has two GNSS stations (ILSU and SJB1). GNSS velocity and displacement time series are obtained from NGL (Blewitt et al., 2018). The GNSS velocities are projected to the LOS direction (Fig. 9).

Water head and precipitation data is provided by the USGS National Water Dashboard and National Water Information System (USGS, n.d.). These datasets contain time series of groundwater levels and total precipitation in some stations (wells) in the study area. I will use these datasets to define in the InSAR time series the expected deformation caused by hydrological loading and poroelastic deformation. Kang and Knight (2023) decomposed the InSAR signals using K-means clustering, this method classifies the different temporal features without any spatial constraints in groups.

- **Preliminary work**

I already processed the InSAR time series for the area between 2016-2022. Here, I am presenting some results relevant to the seasonal signals in the area. For simplicity I will refer to the subsidence to the motions that are negative in the LOS direction and uplift to the motions that are positive in the LOS direction, however, these could include some horizontal component.

The floodings occurred in 2016 between August 11th 14th and led to overflow of the Amite and Comite rivers in the eastern part of the study area (Carney et al., n.d.). Figure 9 shows the apparent effects of the flooding that occurred in 2016 in East Baton Rouge. By March 2016, uplift dominated the southern block of the BR fault. The motion seemed to decrease and there was subsidence for much of the northern block (Fig. 9A). By May, the wet season starts and there is more subsidence in areas near the Amite and Comite Rivers, while the areas near the Mississippi River show uplift (Fig. 9B). By August, when the big storms occurred, most of the area subsided near the three rivers, but there was an area almost in the middle of the study area from NE-SW that showed positive motions (Fig. 9C). By October, almost two months after the storms, the areas near the rivers show subsidence that decreases towards the center of the study area (Fig. 9D).

To this point, it would be possible to assume that most of the seasonality is caused by changes in the hydrological loadings, however, individual time series (Fig. 10) show that wet periods between May and September in areas where the loads should be causing subsidence there are uplift changes too. These time series have not been corrected for reference point motion. The SJB1 GNSS station has a mean velocity in the vertical component of -1.35 mm/y (Blewitt et al., 2018), this velocity is close to the estimates from Wolstencroft et al., (2014) for the area due to long term subsidence processes (GIA and SIA) in the area.

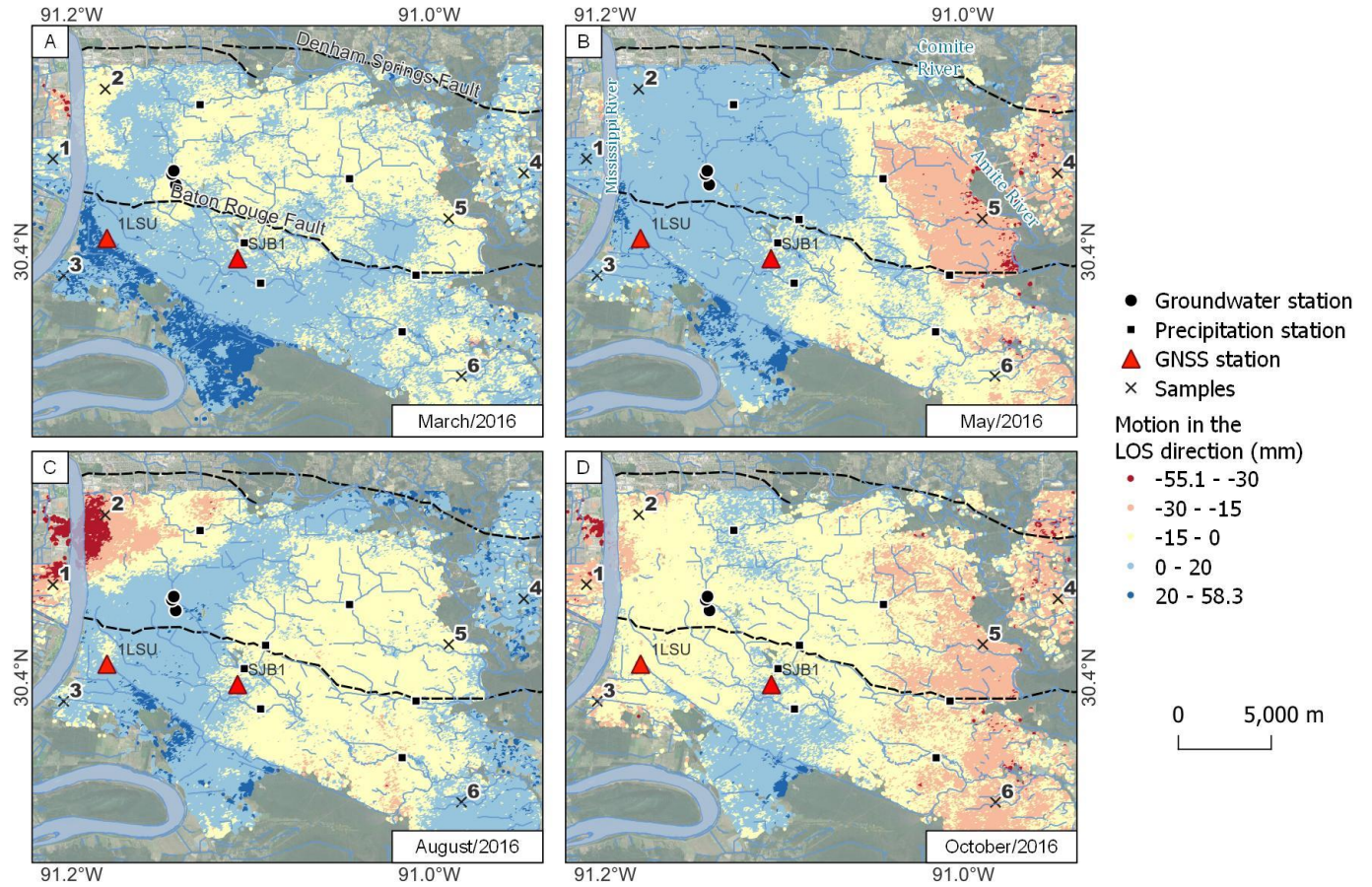


Figure 9: InSAR motions during 2016. Example from InSAR time series to show the spatial changes in motion in the LOS direction during a year of heavy rains. These time series are with reference to the reference point SJB1 and still do not have reference point and plate tectonic motion corrections. Sample points are for time series on Figure 10.

Time series near the Mississippi River (Fig. 10 left column) show that between August and September of 2016, there were negative movements (subsidence) that started to recover in October. The time series near the Amite River (Fig. 10 right column) shows recovery between August and September, and subsidence between September and October. This set of results could be caused by changes in the aquifers that are filled during these months, or by changes in the loads on the rivers, or a mix of both. Another characteristic to notice here is that points near the Mississippi River have time series with larger amplitudes than those in the eastern area near the Amite River.

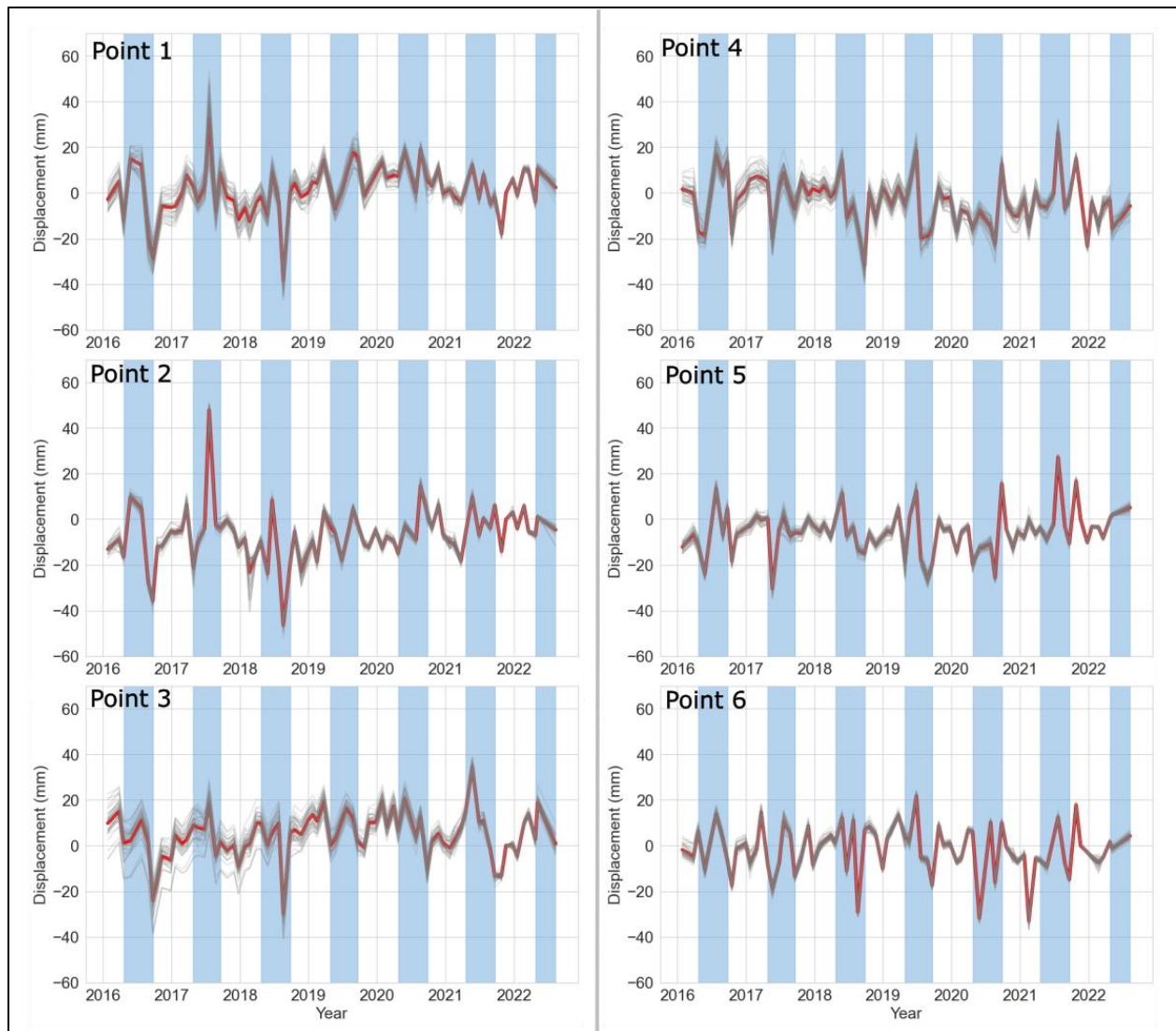


Figure 10: InSAR time series examples (2016 - 2022). The location of these points is on Figure 9. The left column has points near the Mississippi River and the right column has points near the Amite River. These time series are with reference to the reference point (SJB1) and have not been corrected. Red line is the mean value of the gray lines, to calculate these values I took the points in a radius of 250 meters. Each gray line is a point created by SBAS. Blue rectangles are the wet periods between May and September.

- ### Pending Work

These results will be part of a collaborative research. We will compare results and based on the InSAR time series we will be able to implement in the models some corrections to the fault models. I will use precipitation records and groundwater level records to estimate how much subsidence and uplift should be expected from elastic deformation caused by hydrological loads and/or poroelastic deformation caused by recharge of the aquifers in the area. Precipitation and groundwater records are openly available for the stations shown on Figure 9.

APPENDIX - Subsidence variations in coastal East Texas using LiDAR and InSAR time series.

- **Background and goals**

Most of this test study area is in Jefferson County, in coastal Texas (Fig. 11A). Covering the urban areas of Beaumont, Port Neches, Nederland, and Port Arthur with a total area of $\sim 470 \text{ km}^2$, and $\sim 700 \text{ km}^2$ of vegetated and marshland. The study period is limited by the two available LiDAR surveys, the first one was taken in January/2006 (RMSE = 4.8 cm, Point space = unknown) and the second one in February/2017 (RMSE = 8.2 cm, Point space = 0.5 m).

There are several active wells in the region (injection of fluids: 40, extraction of oil-gas: 750, groundwater extraction: 136), this information was obtained from the Railroad Commission of Texas and the Texas Water Development Board. The area is highly vulnerable to sea level rise and rapid subsidence due to natural processes and human-related activities (e.g., Shirzaei and Miller, 2019). Natural processes have a rate of -1.4 mm/y (Zhou et al., 2023). Recent studies have shown that subsidence rates in the area are highly related to population growth, groundwater withdrawal, and oil-gas extraction (Younas et al., 2023). Using GNSS data Younas et al., (2023) estimate that Jefferson County is subsiding at rates between -7.07 to -12.6 mm/y . However, the GNSS stations for that research are in urban areas. The area is also affected by salt domes and growth faults that belong to the Frio fault zone (faults F1 and F2 – Fig. 12) that could be activated by the extraction-injection of fluids.

The purpose of this study is to know what are the limitations of LiDAR methods in a vegetated setting with fewer urban structures. In this case, the precision of LiDAR methods is low due to the vegetation and lack of stable and recognizable surfaces on both LiDAR surveys by ICP. These results are meaningful to illustrate the limitations of using LiDAR on different land covers. Zhong et al., (2022) used LiDAR vertical differencing to estimate changes between the surveys on Eagle Point, Texas. This study is limited to a dense urban region; however, they clip the vegetated areas and do not consider co-registration errors.

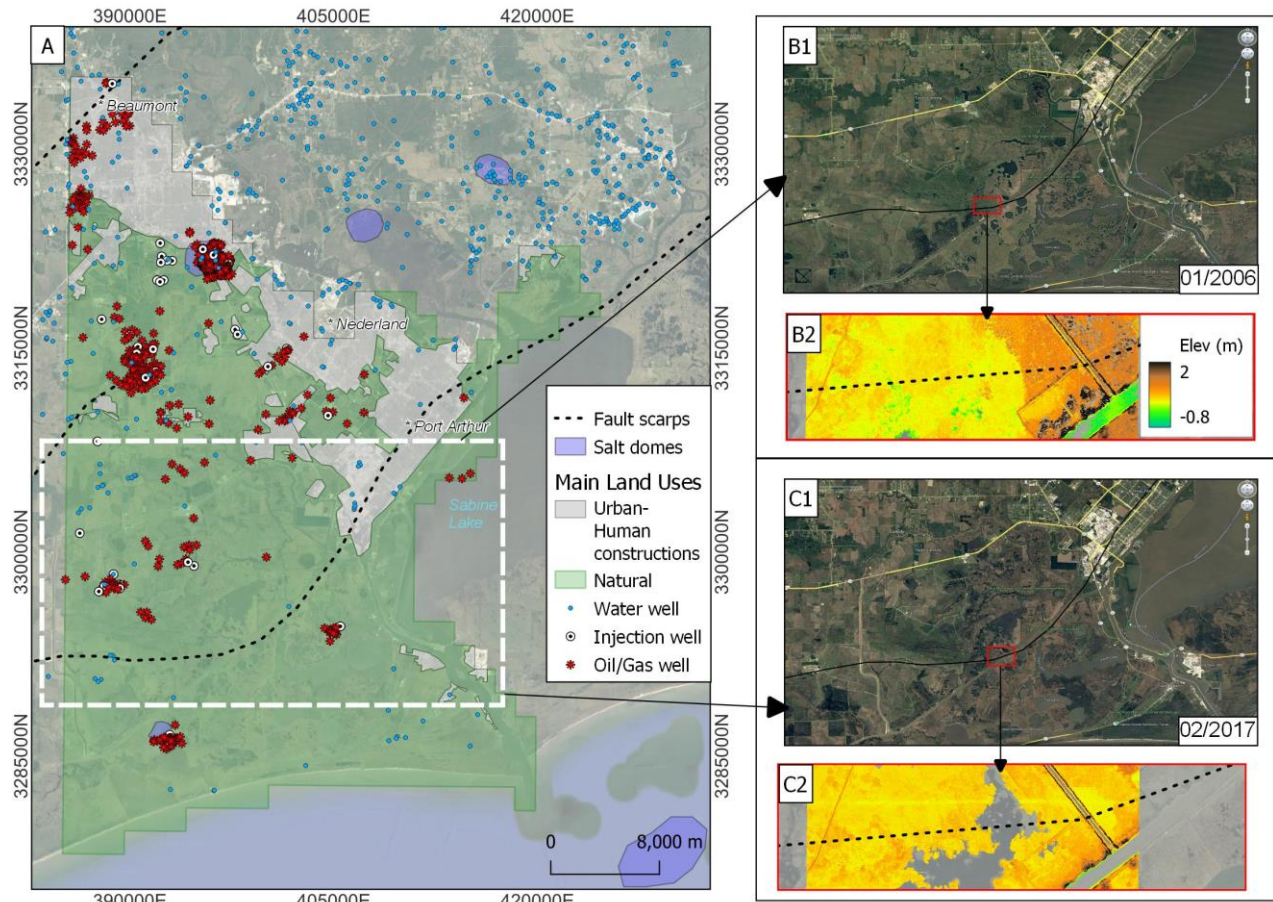


Figure 11: Study area and main features. A) Study area showing the growth faults and salt domes in the area. Injection and oil/gas wells were retrieved from the Railroad Commission of Texas and the water wells from the Texas Water Development Board, white rectangle shows the area in insets B1 and C1 with most of the area covered by natural (vegetated and wetlands). B1) Satellite image from Google Earth showing the area in December 2006 with the fault, B2) DEM created with the LiDAR ground points from the LiDAR survey from 2006, the area covered is shown in B1. C1 and C2 are the same as B1 and B2 but for the 2017 LiDAR survey.

• Results and Conclusions

The entire LiDAR dataset was processed using vertical differencing and ICP. Although these surveys have better point space and smaller RMSE compared to the ones used in the first project the discrepancy between the surveys is large enough to cause visible artifacts. The artifacts were removed by adding/removing a constant from the results, the constants were estimated using several profiles across the area. These results are not tied to a reference ground point, and therefore are not absolute. For easier comparison between urban and natural areas (vegetated and water covered), I digitalized them at a scale of 10,000 these two land uses using the map imagery from QuickMapServices - QGIS (Map data ©2015 Google).

Results in the vertical component with LiDAR ground points (Fig. 12A) indicated that Beaumont is sinking, while Nederland and Port Arthur show some areas of uplift. On the other hand, the results with stable points show an uplift in Beaumont and subsidence near Port Arthur (Fig. 12B). The zone in the middle of the study area (~3300000N, ~397500E) is part of the J.D. Murphree State Wildlife Management Area, in both cases (Fig. 12A and 12B) the area seems to

be sinking, then followed in the south direction by a strip of uplift (or deceleration) closest to the shoreline. These two areas are limited by F2 and F3. Younas et al., (2023) use GNSS data to show that this county is subsiding. It is worth remembering that these results are not tied to a ground reference point, suggesting that uplifting areas are likely subsiding at slower rates than neighboring regions. Horizontal motion is shown in Figure 13. In both cases, for ground and stable surfaces LiDAR points the horizontal motion do not seem to have a clear trend. Displacement with ground LiDAR points (Fig. 13A) shows that the area south of F3 several arrows move towards the East. The arrows in area between the faults F2 and F3 within natural land use start to rotate to northwest, and most arrows between F1 and F3 show motion towards the north. The urban area seems to have larger displacement. Displacement with stable LiDAR points (Fig. 13B) displays slower motions in the complete area and larger errors.

From these preliminary results, I suggest:

- Tying the results to a ground point could benefit the results in *urban areas* to determine whether the vertical motion is fast (Fig. 12A) or slow (Fig. 12B). The tie likely could also determine the real horizontal motion (Fig. 13). In this study case, most of the motion is N-NW, but if the faults are slipping, the motion should be S-SE. These results are in the NAD83 reference frame. The study area has at least seven GNSS stations (Younas et al., 2023), then the comparison between airborne LiDAR methods and GNSS should be more complete for the urban areas than in Baton Rouge.
- *Natural areas* are problematic to handle with this method; Figures 11B1 and 11C1 show that visually the natural area has not had a defined change, meaning that subsidence in this area could be easily masked or hidden by the changes in vegetation and/or vertical accretion of sediments. Figures 11B2 and 11C2 show the DEMs near a fault segment. First, the fault scarp is not seen in either of the DEMs in this area. Second, the elevation does not vary much. This is an obstacle for the ICP algorithm when trying to align the surveys because basically all LiDAR points look too similar to separate any feature, which may explain the spinning-like shapes shown in Figure 13. Last, both DEMs were created with ground LiDAR points, although the terrain in 2006 has less “empty” spots than the one from 2017 where a water body is in the area (Fig. 11B1, B2 C1, C2), this may indicate land loss but not necessarily vertical crustal changes.

For this type of setting an approach similar to the one used by Jankowski et al., (2017) with supporting information from DEMs from different years could be more appropriate. They used 274 Rod surface-elevation table (RSET) across coastal Louisiana to estimate vertical accretion and shallow subsidence. The DEMs could be used to strategically select the sites to install the instruments and reduce the initial amount of fieldwork.

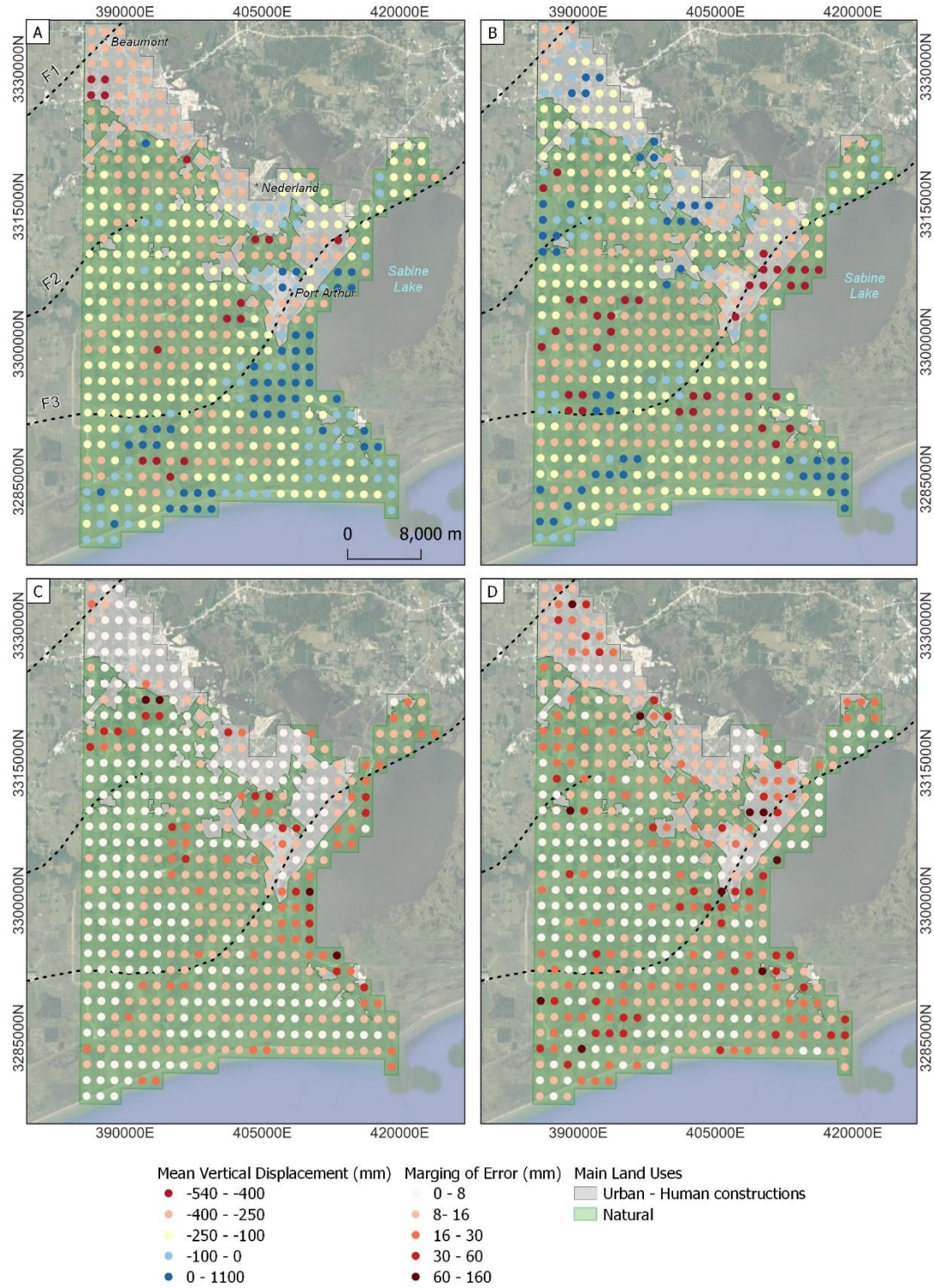


Figure 12: Vertical displacement calculated from ICP algorithm for Jefferson County. (A) Mean displacement using LiDAR ground points. (B) Mean displacement using stable surfaces LiDAR points. (C) Margin of error of the results for (A). (D) Margin of error of the results for (B). Each circle in A and B represents the mean displacement of an area of 2.25 km². Errors in C and D are calculated as the margin of error with respect to the mean. Base map imagery from QuickMapServices - QGIS (Map data ©2015 Google)

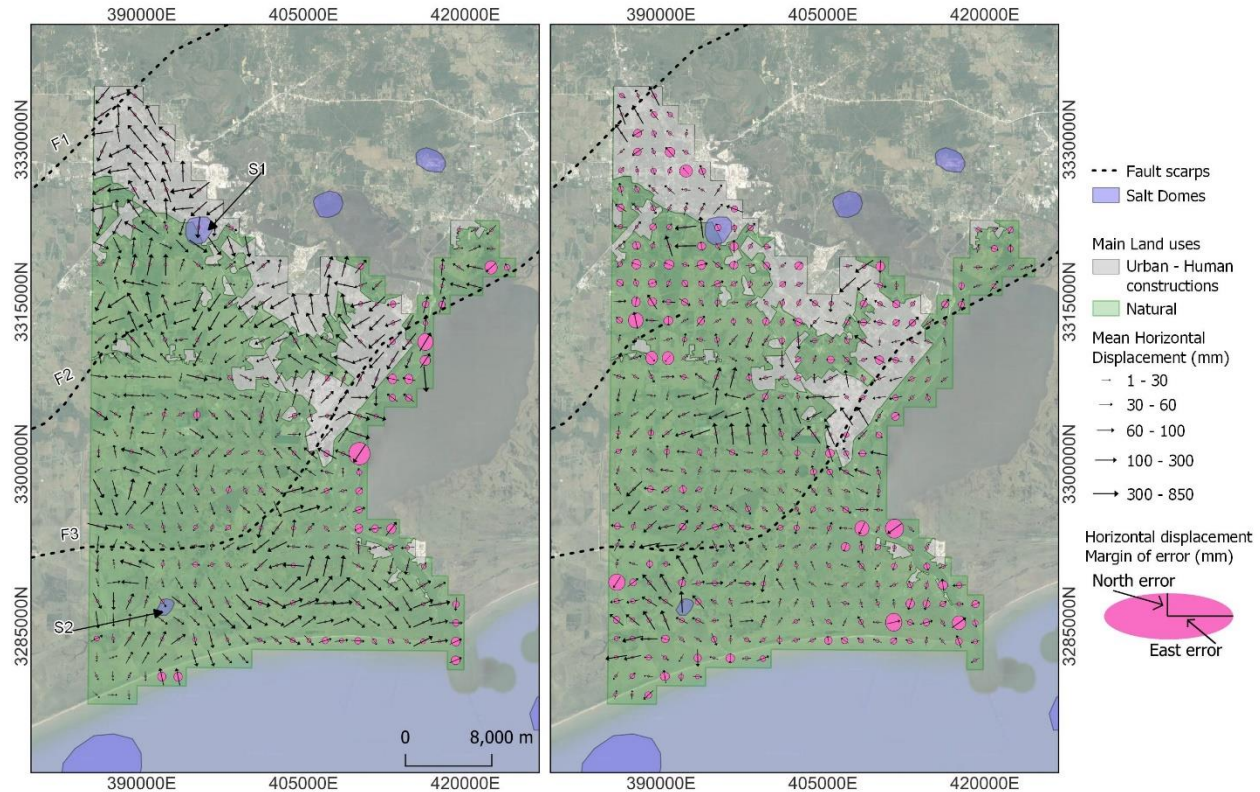


Figure 13: Horizontal displacements calculated with the ICP algorithm. (A) Horizontal displacements using ground LiDAR points. (B) Horizontal displacements using stable surface LiDAR points. Each black arrow represents the average displacement of an area of 2.25 km². Arrow directions represent the mean displacement direction, and the length of the arrow represents the mean displacement magnitude. Ellipses show the error multiplied by 40 for visualization, where East error represents the error in the east component and North error represents the error in the north component. Base map imagery from QuickMapServices - QGIS (Map data ©2015 Google).

RESEARCH TIMELINE

Project and Task	Time
Project 1	This project is already finished and results for publication were re-submitted to the Journal of Geophysical Research - Earth Surface in August/29/2023.
Project 2 <ul style="list-style-type: none"> - Process InSAR time series for the Texas area. - Compare with injection information. - Analysis of the relationship-causation among human activities and earthquakes 	<ul style="list-style-type: none"> - October - November 2023 - January - February 2024 - February - March 2024
Project 3 <ul style="list-style-type: none"> - Collection of data (Precipitation, Groundwater levels) - Analysis of results - Comparison with models 	<ul style="list-style-type: none"> - October 2023 - November 2023– February 2024 - March 2024 (if the models are ready)

REFERENCES

- Anderson, C., Hanor, J., Tsai, F., (2013). Sources of Salinization of the Baton Rouge Aquifer System, Southeastern Louisiana. Gulf Coast Association of Geological Societies Transactions. 63, 3-12.
- Blewitt, G., Hammond, W., Kreemer, C., (2018), “Harnessing the GPS data explosion for interdisciplinary science”. Eos, 99, <https://doi.org/10.1029/2018EO104623>
- Blunden, J., Boyer, T., Eds., (2022). State of the Climate in 2021. Bull. Amer. Meteor. Soc., 103 (8), Si–S465, <https://doi.org/10.1175/2022BAMSStateoftheClimate.1>
- Carney, J., Birch, T., Twilley, R., Wilson, C., Maung-Douglas, K., Pugh, H., Olson, J., Eubanks, K., Karmacharya, R., Chan, Y., (n.d.). LSU – Coastal Sustainability Studio (2016). Baton Rouge, LA. August 2016 – Flood Atlas.
- Chan, A., and Zoback, A., (2007). The Role of Hydrocarbon production on Land Subsidence and fault reactivation in the Louisiana Coastal Zone. *Journal of Coastal Research*, 23 (3), 771-786. doi: 10.2112/05-0553
- Chaussard, E., Burgmann, R., Shirzaei, M., Fielding, E., Baker, B., (2014). Predictability of hydraulic head changes and characterization of aquifer-system and fault properties from InSAR-derived ground deformation. *Journal of Geophysical Research: Solid Earth*. 119 (8), 6572-6590. doi: 10.1002/2014JB011266
- Chen, Y., Vahdat-Aboueshagh, H., Tsai, F., Dausman, A., Runge, M., (2023). Unstructure-grid approach to develop high-fidelity groundwater model to understand groundwater flow and storage responses to excessive groundwater withdrawals in the Southern Hills aquifer system in southeastern Louisiana (USA). *Journal of Hydrology: Regional Studies*. 46. doi: 10.1016/j.ejrh.2023.101342
- Church J., White, N., (2011). Sea-Level Rise from the Late 19th to the early 21st Century. *Surveys in Geophysics*. 32(4-5), 585-602. doi: 10.1007/s10712-011-9119-1
- Crosetto, M., Moserrat, O., Cuevas-Gonzalez, M., Devanthery, N., Crippa, B., (2016). Persistent Scatterer Interferometry: A review. *ISPRS Journal of Photogrammetry and Remote Sensing*. 115, 78-89. doi:10.1016/j.isprsjprs.2015.10.011
- Dokka, R. (2006a). Modern-day tectonic subsidence in Coastal Louisiana. *Geology*. 34 (4), 225-228. doi: 10.1130/G22264.1
- Dokka, R. Sella, G., and Dixon, T. (2006). Tectonic control of subsidence and southward displacement of southeast Louisiana with respect to stable North America: *Geophysical Research Letters*, 33 (L23308). doi:10.1029/2006GL027250
- Dokka, R. (2011). The role of deep processes in late 20th century subsidence of New Orleans and coastal areas of southern Louisiana and Mississippi. *Journal of Geophysical Research*. v. 116 (4), 1-25. doi:10.1029/2010JB008008
- Durham, L., (July 2008). Louisiana Play a 'Company Maker'. AAPG Explorer. Retrieved from: <https://explorer.aapg.org/story/articleid/11008>

- Elshall, A., Tsai, F., Hanor, J., (2013). Indicator geostatistics for reconstructing Baton Rouge aquifer-fault hydrostratigraphy, Louisiana, USA. *Hydrogeological Journal*. 21 (8), p. 1731-1747. doi: 10.1007/s10040-013-1037-5
- Ellsworth, W., (2013). Injection-Induced Earthquakes. *Science*. 341 (1225942). doi: 10.1126/science.1225942
- European Space Agency (ESA) (2021). Copernicus Open Access Hub. Sentinel-1 Images. Last visited February 2023. Retrieved from <https://scihub.copernicus.eu/dhus/#/home>
- Eyre, T., Eaton, D., Garagash, D., Zecevic, M., Venieri, M., Weir, R., Lawton, D., (2019). The role of aseismic slip in hydraulic fracturing-induced seismicity. *Science Advances*. 5. doi: 10.1126/sciadv.aav7172
- Fattahi, H., Amelung, F., (2015). InSAR bias and uncertainty due to the systematic and stochastic tropospheric delay. *Journal of Geophysical Research: Solid Earth*. 120 (12), 87758-87773. doi:10.1002/2015JB012419
- Fiaschi, S., and Wdowinski, S., (2020). Local land subsidence in Miami Beach (FL) and Norfolk (VA) and its contribution to flooding hazard in coastal communities along the U.S. Atlantic coast. *Ocean and Coastal Management*. 187. doi:10.1016/j.ocecoaman.2019.105078
- Frederikse, T., Landerer, F., Caron, L., Adhikari, S., Parkes, D., Humphrey, V., Dangendorf, S., Hogarth, P., Zanna, L., Cheng, L., and Wu, Y., (2020). The causes of sea-level rise since 1900. *Nature*. 584 (7821), 393–397. doi:10.1038/s41586-020-2591-3
- Frohlich, C., Ellsworth, W., Brown, W., Brunt, M., Luetgert, J., MacDonald, T., Walter, S., (2014). The 17 May 2012M4.8 earthquake near Timpson, East Texas: An event possibly triggered by fluid injection. *Journal of Geophysical Research: Solid Earth*. 119, 581-593. doi:10.1002/2013JB010755.
- Gagliano, S., Burton Kemp III, E., Wicker, K., Wiltenmuth, K., and Sabate, R., (2003). Neotectonic framework of southeast Louisiana and applications for Coastal restoration. *Transactions of the 53rd The Gulf Coast Association of Geological Societies and the Gulf Coast Section SEMP*. 262-272
- Gasparini, N, Fischer, G, Adams, J, Dawers, N., Janoff, A., (2015) Morphological signatures of normal faulting in low-gradient alluvial rivers in South-eastern Louisiana, USA. *Earth Surface Processes and Landforms*. 41, 642-657. doi: 10.1002/esp.3852
- Guzy, A., Malinowska, A., (2020). State of the art and recent advancements in the modelling of land subsidence induced by groundwater withdrawal. *Water*. 12 (7). doi:10.3390/w12072051
- Hammes, U., Hamlin, H., Ewing, T., (2011). Geologic analysis of the Upper Jurassic Haynesville Shale in East Texas and West Louisiana. *AAPG Bulletin*. 95 (10), 1643-1666. doi: 10.1306/02141110128

- Hammes, U., Frebourg, S., (2012). Haynesville and Bossier mudrocks: A facies and sequence stratigraphic investigation, East Texas and Louisiana, USA. *Marine and Petroleum Geology*. 31 (1), 8-26. doi: 10.1016/j.marpetgeo.2011.10.001
- Henley, A., (1965). Seismic activity near the Texas Gulf Coast. National Convention. Denver, Colorado: Association of Engineering Geologists.
- Hopkins, M., Lopez, J., Songy, A., (2021). Coastal Subsidence Due to Faults: Insights from Elevation Profiles of Vehicular Bridges, Southeastern Louisiana, U.S.A. *Journal of Coastal Research*. 38(1), 52-65. doi:10.2112/JCOASTRES-D-21-00015.1
- Kang, S., Knight, R., (2023). Isolating the poroelastic response of the groundwater system in InSAR data from the Central Valley of California. *Geophysical Research Letters*. 50 (9). doi: 10.1029/2023GL103222
- Jackson, R., Lowry, E., Pickle, A., Kang, M., DiGiulio, D., Zhao, K., (2015). The depths of hydraulic fracturing and accompanying water use across the United States. *Environmental Science and Technology*. 49 (15), 8969-8976. doi:10.1021/acs.est.5b01228
- Jankowski, K., Törnqvist, T., Fernandes, A., (2017) Vulnerability of Louisiana's coastal wetlands to present-day rates of relative sea-level rise. *Nature Communication*. 8 (14792). doi:10.1038/ncomms14792
- Jones, C., An, K., Blom, R., Kent, J., Ivins, E., and Bekaert, D. (2016). Anthropogenic and geologic influences on subsidence in the vicinity of New Orleans, Louisiana. *Journal of Geophysical Research: Solid Earth*. 121 (5), 3867– 3887. doi:10.1002/2015JB012636
- Karegar, M., Dixon, T., Malservisi, R., Kushe, J., and Engelhart, S., (2017) Nuisance flooding and relative Sea-Level Rise: the importance of present-day land motion. *Science Reports*. 7 (111997). doi:10.1038/s41598-017-11544-y
- Karegar, M., Larson, K., Kushe, J., and Dixon, T., (2020) Novel quantifications shallow sediment compaction by GPS Interferometric Reflectometry and implications for flood susceptibility. *Geophysical Research Letters*. 47 (14). doi:10.1029/2020GL087807
- Keogh, M., and Törnqvist, T., (2019). Measuring rates of present-day relative sea-level rise in low elevation coastal zones. *Ocean Science*, 15 (1), 61-73. doi:10.5194/os-15-61-2019
- Kuchar, J., Milne, G., Wolstencroft, M., Love, R., Taarasov, L., and Hijma, M., (2018). The Influence of Sediment Isostatic Adjustment on Sea Level Change and Land Motion Along the U.S. Gulf Coast: *Journal of Geophysical Research*, 123 (1), 780-796. doi:10.1002/2017JB014695
- Liang, C., Agram, P., Simons, M., Fielding, E., (2019). Ionospheric Correction of InSAR Time Series Analysis of C-Band Sentinel-1 TOPS Data. *IEEE Transactions on Geoscience and Remote Sensing*. 57 (9), 6755-6773. doi: 10.1109/TGRS.2019.2908494
- Love, R., Milne, G., Tarasov, L., Engelhart, S., Hijma, M., Latychev, K., Horton, B., and Törnqvist, T., (2016). The Contribution of Glacial Isostatic Adjustment to projections of Sea-

- level change along the Atlantic and Gulf coast of North America. *Earth's Future*. 4 (10), 440-464. doi:10.1002/2016EF000363
- Louisiana Department of Natural Resources – Strategic Online Natural Resources Information System (SONRIS), (2023). Haynesville shale gas play well Activity map. Last accessed: September/14/2023. Retrieved from: https://www.dnr.louisiana.gov/assets/OC/Energy_exploration_updates/haynesville/hville_WellActivityMap_.pdf
- Mahapatra, P., der Marel, H., van Leijen, F., Samiei-Esfahany, S., Klees, R., Hanssen, R., (2018). InSAR datum connection using GNSS-augmented radar transponders. *Journal of Geodesy*. 92 (1), 21-32. doi:10.1007/s00190-017-1041-y
- Materna, K., Feng, L., Lindsey, E., Hill, E., Ahsan, A., Alam, A., Oo, K., Than, O., Aung, T., Khaing, S., Burgmann, R., (2021). GNSS characterization of hydrological loading in South and Southeast Asia. *Geophysical Journal International*. 224(3) 1742-1752. doi: 10.1093/gji/ggaa500
- Massonnet, D., Feigl, K., (1998). Radar Interferometry and its application to Changes in the Earth's Surface. *Reviews of Geophysics*. 36 (4), 441-500. doi: 10.1029/97RG03139
- Milliner, C., Materna, K., Burgmann, R., Fu, Y., Moore, A., Bekaert, D., Adhikari, S., Argus, D., (2018). Tracking the weight of hurricane Harvey's stormwater using GPS data. *Science advances*. doi: <https://doi.org/10.1126/sciadv.aau2477>
- Morton, R., Busteri, N., Dennis K. (2002). Subsidence Rates and Associated Wetland Loss in South-Central Louisiana. *Transactions of the Gulf Coast Association of Geological Societies*. 52, 767-778.
- Murray, K., Bekaert, D., Lohman, R., (2019). Tropospheric corrections for InSAR: Statistical assessments and applications to the Central United States and Mexico. *Remote Sensing of Environment*. 232. doi: 10.1016/j.rse.2019.111326
- Nasreen, M. (2003) The Effect of Faults upon Ground Water Flow in the Baton Rouge Fault System. [master's thesis]. [New Orleans (LA)] University of New Orleans. Available at <https://scholarworks.uno.edu/td/54> (Accessed: 1 June 2022)
- National Oceanic and Atmospheric Administration (NOAA). Mississippi River Flood History 1543-Present (New Orleans/Baton Rouge). Retrieved from https://www.weather.gov/lix/ms_flood_history
- National Academies of Sciences, Engineering, and Medicine (NASEM), (2018). Thriving on Our Changing Planet: A Decadal Strategy for Earth Observation from Space. Washington, DC: *The National Academies Press*. <https://doi.org/10.17226/24938>.
- Nerem, R., Beckley, B., Fasullo, J., Hamlington, B., Masters, D., Mitchum, G., (2018). Climate-change-driven accelerated sea-level rise detected in the altimeter era. *Proceedings of the National Academy of Sciences*. 115 (9), 2022-2025. doi: 10.1073/pnas.1717312115

- Nienhuis, J., Törnqvist, T., Jankowski, K., Fernandes, A., Keogh, M., (2017). A New Subsidence Map for Coastal Louisiana. *GSA Today*. 27 (9), 58-59. doi:10.1130/GSATG337GW.1
- Nissen, E., Krishnan, A., Arrowsmith, R., Saripalli, S., (2012). Three-dimensional surface displacements and rotations from differencing pre-and post-earthquake LiDAR point clouds. *Geophysical Research Letters*, 39 (16). doi:10.1029/2012GL052460
- Osmanoğlu, B., Sunar, F., Wdowinski, S., Cabral-Cano, E., (2016). Time series analysis of InSAR data: Methods and trends. *ISPRS Journal of Photogrammetry and Remote Sensing*. 115, 90-102. doi: 10.1016/j.isprsjprs.2015.10.003
- PDAL Contributors, (2018). PDAL Point Data Abstraction Library. doi:10.5281/zenodo.2556738
- Penland, S. and Ramsey, K., (1990). Relative Sea Level Rise in Louisiana and the Gulf of Mexico: 1908-1988. *Journal of coastal Research*. 6 (2), 323-342. Available at <https://www.jstor.org/stable/4297682> (Accessed: 20 Marzo 2021)
- Penland, S., Beall, A., and Waters, J., (2001) Environmental atlas of the Lake Pontchartrain Basin. *U.S. Geological Survey*. Open-File Report 02-206. Retrieve from <https://pubs.usgs.gov/of/2002/of02-206/intro/toc.html>
- Puskas, C., Meertens, C., & Phillips, D. (2017). Hydrologic loading model displacements from the National and Global Data Assimilation Systems (NLDAS and GLDAS). UNAVCO Geodetic Data Service Group.
- Railroad Commission of Texas, (2023). Well Layers By County [shapefile format], last visited August/2023. Retrieved from: <https://mft.rrc.texas.gov/link/d551fb20-442e-4b67-84fa-ac3f23ecabb4>
- Rosen, P., Gurrola, E., Sacco, G., Zebker, H., (2011). The InSAR Scientific Computing Environment. *USAR 2012; 9th European Conference on Synthetic Aperture Radar*. p. 730-733
- Rubinstein, J., Mahani, A., (2015). Myths and facts on wastewater injection, hydraulic fracturing, enhanced oil recovery, and induced seismicity. *Seismological Research Letters*. 86 (4). 1060-1067. doi: 10.1785/0220150067
- Samieie-Esfahany, S., Hanssen, R., van Thienen-Visser, K., Muntendam-Bos, A., (2010). On the effect of Horizontal deformation on InSAR subsidence estimates. In *ESA Special Publication*. 677
- Schuler, N., Luttrell, K., (2022). GPS Observations of Subsidence in south Louisiana over seasonal and sub-seasonal timescales associated with Hydrological Loading. [master's thesis and Manuscript in preparation]. [Baton Rouge, LA]. Louisiana State University.
- Scott, C., Arrowsmith, J., Nissen, E., Lajoie, L., Maruyama, T., Chiba, T., (2018). The M7 2016 Kumamoto, Japan, Earthquake: 3-D deformation along the fault and within the damage zone constrained from Differential Lidar Topography. *Journal of Geophysical Research: Solid Earth*, 123 (7) 6138-6155. doi:10.1029/2018JB015581

- Shen, Z., Dawers, N., Törnqvist, T., Gasparini, N., Hijma, M., and Mauz, B. (2017). Mechanism of late Quaternary fault throw-rate variability along the north central Gulf of Mexico coast: implication for coastal subsidence. *Basin Research*. 29 (5), 557-570. doi:10.1111/bre.12184
- Shirzaei, M., Ellsworth, W., Tiampo, K., Gonzalez, P., Manga, M., (2016). Surface uplift and time-dependent seismic hazard due to fluid injection in eastern Texas. *Science*. 353 (6306), 1416-1419. doi:10.1126/science.aag0262
- Shirzaei, M., Miller, M., (2019). Land subsidence in Houston correlated with flooding from Hurricane Harvey. *Remote Sensing of Environment*. 225. doi: 10.1016/j.rse.2019.03.022
- Shirzaei, M., Freymuller, J., Tornqvist, T., Galloway, D., Dura, T., Minderhoud, P., (2021). Measuring, modeling and projecting coastal land subsidence. *Nature Reviews Earth and Environment*. 2(1), 40-58. doi: 10.1038/s43017-020-00115-x
- Speight, J., (2020). Chapter 2 – Resources. In J. Speight (Ed.). *Shale Oil and Gas Production Processes* (65-138). Gulf Professional Publishing. <https://doi.org/10.1016/B978-0-12-813315-6.00002-6>
- Stephenson, O., Liu, Y., Zhang, Y., Simons, M., Rosen, P., Xu, X., (2022). The Impact of Plate Motions on Long-Wavelength InSAR-Derived Velocity Fields. *Geophysical Research Letters*. 49(21). doi: 10.1029/2022gl099835
- Stevenson, D., McCulloh, R., (2001). Earthquakes in Louisiana. Louisiana Geological Survey. Public information series n. 7. Available at https://www.lsu.edu/lgs/publications/products/Free_publications/La-earthquakes.pdf (Accessed: August 2023)
- Texas Water Development Board (2021). Groundwater Database (GWDB) Well Location Shapefile [Shapefile format], last visited October/2021. Retrieve from: <https://www.twdb.texas.gov/groundwater/data/gwdbbrpt.asp#GWDBDownloads>
- Tomaszewski, D., Lovelace, J., Ensminger, P., (2002). Water withdrawals and trends in groundwater levels and stream discharge in Louisiana. Louisiana Department of Transportation and Development, and U.S. Geological Survey, technical report No. 68.
- United States Army Corps of Engineers (USACE) (2001). Data from: Raw LIDAR Elevation Data, UTM 15 NAD83, Louisiana FEMA Project - Phase 1: Amite River Basin. [xyz format] last visited June/2020 Retrieve from: <https://maps.ga.lsu.edu/lidar2000/>
- United States Geological Survey (USGS) (2019), National Water Dashboard. Precipitation time series. Last visited October/2022. Retrieve from: <https://dashboard.waterdata.usgs.gov/app/nwd/en/?region=lower48&aoi=default>
- United States Geological Survey (USGS) (2019), National Water Information System. Groundwater levels time series and locations. Last visited October/2022. Retrieve from: <https://dashboard.waterdata.usgs.gov/app/nwd/en/?region=lower48&aoi=default>

- United States Geological Survey (USGS) (2019), USGS Lidar Point Cloud LA Amite 2018, [LAZ format], last visited July/2022. Retrieve from:
https://rockyweb.usgs.gov/vdelivery/Datasets/Staged/Elevation/LPC/Projects/USGS_LPC_LA_Amite_2018_LAS_2019/
- Vahdat-Aboueshagh, H., Tsai, F., (2021). Constructing large-scale complex aquifer systems with big well log data: Louisiana model. *Computers and Geosciences*. 148, 104687. doi:10.1016/j.cageox.2021.104687
- Walter, J., Dotray, P., Frohlich, C., Gale, J., (2016). Earthquakes in northwest Louisiana and the Texas–Louisiana border possibly induced by energy resource activities within the Haynesville shale play. *Seismological Research Letters*. 87 (2A), 285-294. doi: 10.1785/0220150193
- Weingarten, M., Ge, S., Godt, J., Bekins, B., Rubinstein, J., (2015). High-rate injection is associated with the increase in U.S. mid-continent seismicity. *Science*. 348 (6241). 1336-1340. doi: 10.1126/science.aab1345
- Wheaton, J., Brasington, J., Darby, S., Sear, D., (2010). Accounting for uncertainty in DEMs from repeat topographic surveys: improved sediment budgets. *Earth Surface processes and Landforms*. 35 (2), 136-156. doi:10.1002/esp.1886 [computer software]
<https://github.com/Riverscapes/gcd>
- Wheaton, J., (2018). Principles of topographic change detection. *EarthCube Advancing the Analysis of HRT Workshop Advancing the Analysis of High-Resolution Topography*, Broomfield, CO. August 21-24.
https://www.youtube.com/watch?v=QIoK52W5sUM&ab_channel=OpenTopography (last accessed November 10, 2020).
- Wheeler, R., Heinrich, P., compilers, (1998). Fault number 1022, Gulf-margin normal faults, Louisiana and Arkansas, in Quaternary fault and fold database of the United States. U.S. Geological Survey website. Last accessed: September 8, 2023.
- White, E. (2017). Water Resources of the Southern Hills Regional Aquifer System, Southeastern Louisiana. U.S. Geological Survey Fact Sheet 2017–3010. doi:10.3133/fs20173010
- White, A., Gardner, W., Borsa, A., Argus, D., Martens, H., (2022). A Review of GNSS/GPS in hydrogeodesy: Hydrologic loading applications and their implications for water resource research. *Water Resources Research*. 58 (7). doi: 10.1029/2022WR032078
- Wolstencroft, M., Shen, Z., Törnqvist, T., Milne, G., Kulp, M., (2014). Understanding subsidence in the Mississippi Delta region due to sediment, ice and ocean loading: Insights geophysical modeling. *Journal of Geophysical Research: Solid Earth*. 119 (4), 3838-3856. doi: 10.1002/2013JB010928
- Xia, Y., (2010). Synthetic Aperture Radar Interferometry. In G. Xu (Ed.). *Sciences of Geodesy-1: Advances and Future Directions* (p. 416 - 473). doi: 10.1007/978-3-642-11741-1

- Younas, M., Khan, S., Tirmizi, O., Hamed, Y., (2023). Geospatial analytics of driving mechanism of land subsidence in Guld Coast of Texas, United States. *Science of the Total Environment*. 902. doi: 10.1016/j.scitotenv.2023.166102
- Yunjun, Z., Fattahi, H., Amelung, F., (2019). Small baseline InSAR time series analysis: Unwrapping error correction and noise reduction. *Computers and Geosciences*. 133. doi: 10.1016/j.cageo.2019.104331.
- Zhong, W., Chu, T., Tissot, P., Wu, Z., Chen, J., Zhang, H., (2022). Integrated coastal subsidence analysis using InSAR, LiDAR and land cover data. *Remote Sensing of Environment*. 282. doi: 10.1016/j.rse.2022.113297
- Zhou, X., Wang, G., Wang, K., Liu, H., Lyu, H., Turco, M., (2023). Rates of natural subsidence along the Texas Coast derived from GPS and tide gauge measurements. *Journal of Surveying Engineering – Preprint*. 147 (4). doi: 10.13140/RG.2.2.26974.97606